國立臺灣大學理學院物理學系

碩士論文

Department of Physics
College of Science
National Taiwan University

Master Thesis

水球體與水二聚體微波加熱之極化電荷屏蔽效應與共振現象

Effects of Polarization Charge Shielding and Resonance in Microwave Heating of Water Sphere and Dimer

梁如青

Ju-Ching Liang

指導教授：朱國瑞 博士

Advisor: Kwo-Ray Chu, Ph.D.

中華民國 112 年 6 月

June, 2023

doi:10.6342/NTU202300933

國立臺灣大學碩士學位論文
口試委員會審定書
MASTER'S THESIS ACCEPTANCE CERTIFICATE
NATIONAL TAIWAN UNIVERSITY

水球體與水二聚體微波加熱之極化電荷屏蔽效應與共振現象

Effects of Polarization Charge Shielding and Resonance in Microwave Heating of Water Sphere and Dimer

本論文係梁如青（R10222027）在國立臺灣大學理學院物理學系完成之碩士學位論文，於民國 112 年 6 月 2 日承下列考試委員審查通過及口試及格，特此證明。

The undersigned, appointed by the Department of Physics on 06/02/2023 have examined a Master's thesis entitled above presented by Ju-Ching Liang (R10222027) candidate and hereby certify that it is worthy of acceptance.

口試委員 Oral examination committee:

朱國瑞　陳仕豪　張存續

（指導教授 Advisor）

陳漢穎　姜暐元

系主任/所長 Director: 理學院物理系暨研究所系主任/所長

致謝

求學之路在此畫下句點，一路上擁有許多人的幫助和陪伴，著實幸運。

在這間實驗室的兩年多裡，我學到了許多，感謝朱老師的指導，提供了許多研究的方向。剛進到實驗室時我很茫然，面對從未接觸的物理研究感到非常恐懼，謝謝立中不只在電磁模擬和研究方面一步一步帶領我，好像遇到困難時立中總有解決辦法，在我焦慮的時候也總是告訴我沒問題。

北漂了近六年，對於很依賴情感的我來說，隻身在陌生的台北是一大挑戰，更別說面對未知的大學和研究生活。謝謝 Sven 幾年的陪伴，在無數個焦慮和崩潰的時刻都給我鼓勵和安定感，也謝謝以前的 102 團、後來的 DLC 群。謝謝前室友唯中和曉嵐，大學時代在寢室天南地北的聊天也是在台北的珍貴記憶之一。謝謝教育學程的大家，在這條路上遇到很多不一樣的人，也創造了很多快樂的回憶。謝謝胖胖和芯寶，在我一個人在寢室時常常找我聚餐聊天。

除了在台北的人們之外，台中也有一群非常重要的人。謝謝忠義一路的陪伴，在我感到茫然的時候聽我說話，也從不吝給予我支持和鼓勵，成為我心中發光的存在。謝謝冠冠、少爺團、Funky、芷瑄，高中建立的情誼一直維持到現在。最後也最重要的，是一直以來家人的支持和陪伴。謝謝拔麻對我的人生給予很大的自由，從選讀物理系、教育學程至今也一直支持著我，在我北漂想家時總是說，那就回家吧。謝謝哥哥們、大嫂、宸軒、景翔，每次回家時都讓家充滿笑聲，讓家成為我放肆大笑的地方。非常感謝家人們，讓家一直是我的避風港。

2023.06.02 梁如青

doi:10.6342/NTU202300933

中文摘要

介電質微波加熱是多年來常見的科學研究議題，也被廣泛應用在工業領域，又以水為最具代表性的介電質材料之一。其中，微波加熱的速率和介電質內部電場強度有高相關性。然而，影響介電質內部電場分布的物理成因卻較少被研究。本論文著重探討兩個主要的成因：共振與極化電荷屏蔽效應，以及在水球體和水二聚體中，兩者如何交互作用以影響電場分布。其中，本論文主要以數學解析解分析水單球體的電場，並以文獻回顧探討水二聚體內部及間隙電場。本論文指出，對於水單球體而言，介電質內部電場強度及分布隨球體尺寸改變而有所不同。共振效應只在球體尺寸與電磁波波長相近時有顯著影響，而極化電荷屏蔽效應則廣泛存在於不同尺寸的球體中。對於水二聚體而言，間隙之電場因間隙兩側的極化電荷互相影響而顯著增強，但共振效應仍獨立存在於兩個球體內部。本論文對介電質球體在微波中的物理機制有基本理解，亦可呼應其他文獻的研究結果。

關鍵詞：介電質微波加熱、極化電荷屏蔽效應、微波共振、介電質球狀共振腔、平面波、間隙電場強化作用

doi:10.6342/NTU202300933

Effects of Polarization Charge Shielding and Resonance in Microwave Heating of Water Sphere and Dimer

Ju-Ching Liang

Advisor: Kwo-Ray Chu, Ph.D.

Department of Physics

National Taiwan University

Taipei, Taiwan

June, 2023

doi:10.6342/NTU202300933

Abstract

Microwave dielectric heating has long been a topic of scientific researches and a technique in industrial applications, with water being one of the most representative materials. It is also well known that the microwave heating rate has a high dependency on the electric field strength inside the dielectric. However, the physical origins determining the interior electric field pattern have not been studied as much. This thesis focuses on two primary effects, resonance and polarization charge shielding effect, as well as how they interact to form the interior electric field of a water sphere and dimer. In this thesis, analytical analysis is used to analyze the field profiles for single water sphere, while literature review is the main research method for water dimer. For single water sphere, it is shown that the electric field strength and uniformity is highly dependent on the dimension of the sample. The resonant effect is only significant when the dimension of the object is of the same order as the wavelength, whereas the polarization charge shielding effect can be observed in a wider size range. For water dimers, the gap field is significantly enhanced by polarization charges from gap-sides of both spheres, whereas the resonance in each sphere is independent from each other. This thesis gives basical understanding to the behavior of dielectric spheres under microwaves, and is consistent with the results from further researches.

Keywords: Microwave dielectric heating; Polarization charge shielding effect; Microwave resonance; Dielectric spherical resonator; Plane wave; Gap electric field enhancement

doi:10.6342/NTU202300933

Contents

Abstract i

List of Figures iv

List of Tables vi

1 Introduction 1

2 Normal Modes Analysis of a Spherical Water Resonator: Analytical Result 4

2.1 Theory 4

2.2 Methods 9

2.3 Results and Discussion 9

3 A Water Sphere Hit by a 2.45 GHz Plane Wave: Analytical Analysis 19

3.1 Theory 19

3.2 Methods 23

3.3 Results and Discussion 23

3.3.1 Field Analysis: Comparison with Normal Mode 24

3.3.2 Field Analysis: General Dependency on Water Sphere Radius . . 25

4 Gap Fields between Water Dimers Hit by Plane Waves 30

5 Conclusion 37

doi:10.6342/NTU202300933

Appendices **39**

A Helmholtz Equation and Its Solution **39**

A.1 Scalar Helmholtz Equation and Its Solution 39

A.2 Vector Helmholtz Equation and Its Solution 40

Reference **42**

doi:10.6342/NTU202300933

List of Figures

2.1 The complex dielectric constant of water at $25\,^{\circ}\mathrm{C}$ as a function of frequency. 10

2.2 The normalized color scale for field profiles in Section 2.3. 10

2.3 Electric field profiles of TE_{n01} modes. 12

2.4 Magnetic field profiles of TE_{n01} modes. 12

2.5 Electric field profiles of TM_{n01} modes. 13

2.6 Magnetic field profiles of TM_{n01} modes. 13

2.7 Electric field profiles of TE_{2m1} modes. 14

2.8 Magnetic field profiles of TE_{2m1} modes. 14

2.9 Electric field profiles of TM_{2m1} modes. 15

2.10 Magnetic field profiles of TM_{2m1} modes. 15

2.11 Electric field profiles of TE_{10q} modes. 17

2.12 Magnetic field profiles of TE_{10q} modes. 17

2.13 Electric field profiles of TM_{10q} modes. 18

2.14 Magnetic field profiles of TM_{10q} modes. 18

3.1 Electric field profiles for a water sphere of radius $6.8\,\mathrm{mm}$ in three circumstances. 26

3.2 $\overline{A}$ and σ_A as functions of R showing the behavior of both in three regimes. 28

3.3 Electric field profiles on the xy-plane for a water sphere of four radii hit by a $2.45\,\mathrm{GHz}$ uniform plane wave. 28

doi:10.6342/NTU202300933

3.4 Electric field profiles on the xz-plane for a water sphere of four radii hit by a $2.45\,\mathrm{GHz}$ uniform plane wave. 29

4.1 Simulation model of a water dimer composed of two water spheres with $R = 7\,\mathrm{mm}$ separated by a variable gap width d, based on Lin *et al.* [1], Fig. 2a. 31

4.2 Simulation results at $27\,\mathrm{MHz}$ polarized at x-axis under $E_{ext} = 400\,\mathrm{V/cm}$ for different dimer orientations (both with $d = 0.5\,\mathrm{mm}$), based on Lin *et al.* [1], Fig. 2c and Fig. 2g. 32

4.3 Simulation results at $27\,\mathrm{MHz}$ polarized at x-axis under $E_{ext} = 400\,\mathrm{V/cm}$ for different gap widths d, based on Lin *et al.* [1], Fig. 2d and Fig. 2e. . . 33

4.4 Experiment results of the hydrogel dimer with three values of gap width d in a $27\,\mathrm{MHz}$ capacitor, where $E_{ext} = 400\,\mathrm{V/cm}$ and the exposure time is $35\,\mathrm{s}$, based on Lin *et al.* [1], Fig. 3b and Fig. 3d. 34

4.5 Simulation results of a water dimer with three gap distances d at $2.45\,\mathrm{GHz}$ polarized at x-axis under $E_{ext} = 400\,\mathrm{V/cm}$, based on Lin *et al.* [1], Fig. 6b and Fig. 6c. 35

4.6 Experiment results of the hydrogel dimer with three values of gap width d placed in front of a $2.45\,\mathrm{GHz}$ antenna, where $E_{ext} = 100\,\mathrm{V/cm}$ and the exposure time is $10\,\mathrm{s}$, based on Lin *et al.* [1], Fig. 7a and Fig. 7b. 36

4.7 Simulated gap field amplitudes as functions of frequency for different gap widths d, based on Lin *et al.* [1], Fig. 5a and Fig. 5b. 36

doi:10.6342/NTU202300933

List of Tables

2.1 Properties of TE and TM modes. 5
2.2 Parameters of Eq. (2.24) at different temperatures [2]. 10
2.3 Water sphere radius at 2.45 GHz for each normal mode. 11

doi:10.6342/NTU202300933

Chapter 1

Introduction

Dielectric heating by microwave has been widely used in various research fields and industrial applications, such as insect control [3, 4], food industry [5–7], and sintering [8–10]. Microwave region ranges from $300\,\mathrm{MHz}$ to $300\,\mathrm{GHz}$ with wavelength ranging from $1\,\mathrm{mm}$ to $1\,\mathrm{m}$ [11]. In practical cases, dielectric materials are incident by an external electromagnetic wave, absorbing energy from electromagnetic wave fields. For a dielectric object with complex permittivity ε expressed as

$$\varepsilon/\varepsilon_0 = \varepsilon' + i\varepsilon'' \quad (\varepsilon', \varepsilon'' \in \mathbb{R}), \tag{1.1}$$

its time-averaged power absorption rate P_{loss} from an electromagnetic wave is given by [12]

$$P_{loss} = \frac{1}{2}\omega \,\mathrm{Im}(\varepsilon)|\boldsymbol{E}_{in}|^2 \tag{1.2}$$

where ω is the frequency of the electromagnetic wave and $\boldsymbol{E}_{in}$ is the electric field inside the dielectric. Eq. (1.2) suggests that the field strength inside the dielectric is the key to higher heating rate. Hence, it is essential to understand the mechanism of generating the internal field. Aside from the external field strength, there are two main factors affecting the internal electric field: *Polarization Charge Shielding Effect* and *Resonance*.

When a dielectric object immerses in an electric field, the bound molecular charges will be slightly displaced to form polarization charges, preventing the external electric

doi:10.6342/NTU202300933

field from penetrating inside the medium. Hence, polarization charge shielding effect causes the internal field to be weaker. This is a widely known effect often introduced Electromagnetism textbooks [13, 14]. Secondly, when a dielectric object is excited by electromagnetic waves with specific wavelengths, the wave interference between incident and reflected waves determines the field strength inside the object. At specific wavelengths, with constructive interference, the field inside the object with large amplitude has the most energy, here called *resonance*, and the dielectric object is then called an "resonator". Focusing on a dielectric sphere, a common shape used in various applications, there are quite a few literatures developing thorough research on the internal field [15, 16], while the external field has been less focused.

These two effects has long been studied separately. However, practically they take effect simultaneously to generate the total electric field. Hence, they should be studied at once to observe the total effect. Moreover, in some application (e.g., sintering), large quantities of dielectric objects are heated together. The electric field in between could play an important role. This indicates that the external fields caused by polarization charge shielding effect and resonances are worth studying. More deeply, directly studying the field between closely placed dielectric spheres has a high practical value [1].

The first aim of this thesis is to present both internal and external field patterns of a dielectric sphere resonator. Chapter 2 focuses on analytic solutions of the resonant fields of a dielectric sphere resonator.

The second aim of this thesis is to study the composite effects caused by polarization charge shielding and resonances through analytical analysis and literature review. It is difficult to isolate each effect from the electric field pattern, but the physical origin of field properties can be identified. Besides, among a variety of dielectric materials, water is one of the most useful and studied substances in scientific research and microwave applications [17–19]. Hence, the dielectric of interest in this thesis is chosen to be water as well. Chapter 3 studies the field properties for water spheres of different radii. Chapter 4

doi:10.6342/NTU202300933

summarizes the paper of Lin *et al*. [1] to understand the gap field properties of a water dimer.

doi:10.6342/NTU202300933

Chapter 2

Normal Modes Analysis of a Spherical Water Resonator: Analytical Result

Before analyzing the fields of water sphere(s) with incident wave, it is crucial to understand resonant modes of a spherical water resonator. In this chapter, Section 2.1 derives the analytic solutions to the spherical dielectric resonator problem; Section 2.3 provides field profiles of first few modes.

2.1 Theory

Consider a dielectric sphere of radius R with permeability μ_0 and complex permittivity ε, where $\varepsilon/\varepsilon_0 = \varepsilon' + i\varepsilon''$ ($\varepsilon', \varepsilon'' \in \mathbb{R}$). With the assumption $E, H \sim e^{-i\omega t}$ [20], fields inside the sphere (denoted by the superscript"-") satisfy the source-free Maxwell's equations

$$\begin{cases} \boldsymbol{\nabla} \cdot \boldsymbol{E}^- = 0, & \boldsymbol{\nabla} \times \boldsymbol{E}^- = ikZ\boldsymbol{H}^- \\ \boldsymbol{\nabla} \cdot \boldsymbol{H}^- = 0, & \boldsymbol{\nabla} \times \boldsymbol{H}^- = -ik\boldsymbol{E}^-/Z \end{cases}, \quad \text{for } r < R \tag{2.1}$$

where the wavenumber $k = \sqrt{\varepsilon\mu_0}\,\omega$ and the wave impedance $Z = \sqrt{\mu_0/\varepsilon}$. Combining the two curl-equations, Eq. (2.1) can be expressed as

$$\left(\nabla^2 + k^2\right)\boldsymbol{E}^- = 0, \quad \boldsymbol{\nabla} \cdot \boldsymbol{E}^- = 0, \quad \text{with } \boldsymbol{H}^- = -\frac{i}{kZ}\boldsymbol{\nabla} \times \boldsymbol{E}^- \tag{2.2}$$

doi:10.6342/NTU202300933

	Field characteristic	Boundary condition
TE mode	$E_r = 0$ everywhere	$(\partial B_r/\partial n)\|_S = 0$
TM mode	$B_r = 0$ everywhere	$E_r\|_S = 0$

Table 2.1: Properties of TE and TM modes.

or

$$\left(\nabla^2 + k^2\right)\boldsymbol{H}^- = 0, \quad \boldsymbol{\nabla}\cdot\boldsymbol{H}^- = 0, \quad \text{with } \boldsymbol{E}^- = \frac{iZ}{k}\boldsymbol{\nabla}\times\boldsymbol{H}^-. \tag{2.3}$$

Hence, both $\boldsymbol{E}^-$ and $\boldsymbol{H}^-$ are transverse solutions to a vector Helmholtz equation, the exact solutions can be obtained by applying boundary conditions to Eqs. (A.13b) and (A.13c). Since the fields are finite everywhere inside the sphere, $Q_n^m(\cos\theta)$ and $y_n(kr)$ should be dropped due to their singularities at $\cos\theta = \pm 1$ and $r = 0$, i.e. the solution of ψ to Eq. (A.1) can be set as

$$\psi^- = j_n(kr)P_n^m(\cos\theta)e^{im\phi}. \tag{2.4}$$

As for the fields outside the sphere (denoted by the superscript "+"), they as well satisfy Eqs. (2.1) – (2.3), with k and Z replaced by $k_0 = \omega/c$ and $Z_0 = \sqrt{\mu_0/\varepsilon_0}$, respectively. The boundary conditions for fields outside the sphere are slightly different from those inside the sphere. Not only should they remain finite everywhere, they should also take the form of an outgoing wave as $r \to \infty$, i.e.,

$$\psi^+(r \to \infty) \sim e^{ik_0 r}. \tag{2.5}$$

Thus, ψ^+ can be set as

$$\psi^+ = h_n^{(1)}(k_0 r)P_n^m(\cos\theta)e^{im\phi} \tag{2.6}$$

where $h_n^{(1)}(k_0 r)$ is the spherical hankel function of the first kind.

Resonant modes can be divided into two categories: *Transverse Electric (TE) modes* and *Transverse Magnetic (TM) modes* [21], the properties of which are shown in Table 2.1.

doi:10.6342/NTU202300933

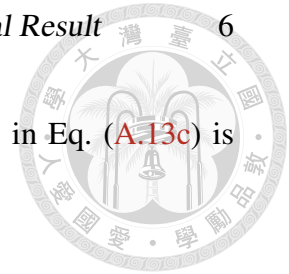

Starting with TE modes, since $E_r = 0$ everywhere, function $\boldsymbol{N}$ in Eq. (A.13c) is eliminated. Then the fields can be described by

$$\boldsymbol{E}^-_{TE} = A_{nm}\boldsymbol{M}^-_{nm}(\boldsymbol{r}, k), \qquad \boldsymbol{H}^-_{TE} = -\frac{i}{kZ}\boldsymbol{\nabla}\times\boldsymbol{E}^-_{TE} \qquad \text{for } r < R; \tag{2.7}$$

$$\boldsymbol{E}^+_{TE} = B_{nm}\boldsymbol{M}^+_{nm}(\boldsymbol{r}, k_0), \qquad \boldsymbol{H}^+_{TE} = -\frac{i}{k_0 Z_0}\boldsymbol{\nabla}\times\boldsymbol{E}^+_{TE} \qquad \text{for } r > R \tag{2.8}$$

where

$$\begin{aligned}\boldsymbol{M}^-_{nm}(\boldsymbol{r}, k) &= \boldsymbol{\nabla}\times\left(kr\psi^-\right)\hat{\boldsymbol{r}} \\ &= \left[\frac{1}{r\sin\theta}\frac{\partial}{\partial\phi}\hat{\boldsymbol{\theta}} - \frac{1}{r}\frac{\partial}{\partial\theta}\hat{\boldsymbol{\phi}}\right] krj_n(kr)P^m_n(\cos\theta)e^{im\phi},\end{aligned} \tag{2.9}$$

$$\begin{aligned}\boldsymbol{M}^+_{nm}(\boldsymbol{r}, k_0) &= \boldsymbol{\nabla}\times\left(k_0 r\psi^+\right)\hat{\boldsymbol{r}} \\ &= \left[\frac{1}{r\sin\theta}\frac{\partial}{\partial\phi}\hat{\boldsymbol{\theta}} - \frac{1}{r}\frac{\partial}{\partial\theta}\hat{\boldsymbol{\phi}}\right] k_0 rh^{(1)}_n(k_0 r)P^m_n(\cos\theta)e^{im\phi}\end{aligned} \tag{2.10}$$

with a factor k and k_0 inserted respectively for consistency, and A_{nm}, B_{nm} are some constants. Hence, the electric field components are given by

$$E^-_{TE,r} = 0, \tag{2.11a}$$

$$E^-_{TE,\theta} = iA_{nm}mkj_n(kr)\frac{P^m_n(\cos\theta)}{\sin\theta}e^{im\phi}, \tag{2.11b}$$

$$E^-_{TE,\phi} = A_{nm}kj_n(kr)\sin\theta P^{m'}_n(\cos\theta)e^{im\phi}; \tag{2.11c}$$

$$E^+_{TE,r} = 0, \tag{2.12a}$$

$$E^+_{TE,\theta} = iB_{nm}mk_0h^{(1)}_n(k_0 r)\frac{P^m_n(\cos\theta)}{\sin\theta}e^{im\phi}, \tag{2.12b}$$

$$E^+_{TE,\phi} = B_{nm}k_0h^{(1)}_n(k_0 r)\sin\theta P^{m'}_n(\cos\theta)e^{im\phi}. \tag{2.12c}$$

doi:10.6342/NTU202300933

The magnetic field components are given by

$$\begin{aligned} H^-_{TE,r} &= -\frac{iA_{nm}j_n(kr)}{Zr} \\ &\quad \left[-\sin^2\theta P_n^{m''}(\cos\theta) + 2\cos\theta P_n^{m'}(\cos\theta) + \frac{m^2}{\sin^2\theta}P_n^m(\cos\theta)\right]e^{im\phi} \\ &= -\frac{iA_{nm}n(n+1)}{Zr}j_n(kr)P_n^m(\cos\theta)e^{im\phi}, \end{aligned} \tag{2.13a}$$

$$H^-_{TE,\theta} = \frac{iA_{nm}}{Zr}[j_n(kr) + krj_n'(kr)]\sin\theta P_n^{m'}(\cos\theta)e^{im\phi}, \tag{2.13b}$$

$$H^-_{TE,\phi} = \frac{A_{nm}m}{Zr}[j_n(kr) + krj_n'(kr)]\frac{P_n^m(\cos\theta)}{\sin\theta}e^{im\phi}; \tag{2.13c}$$

$$H^+_{TE,r} = -\frac{iB_{nm}n(n+1)}{Z_0r}h_n^{(1)}(k_0r)P_n^m(\cos\theta)e^{im\phi}, \tag{2.14a}$$

$$H^+_{TE,\theta} = \frac{iB_{nm}}{Z_0r}\left[h_n^{(1)}(k_0r) + k_0rh_n^{(1)'}(k_0r)\right]\sin\theta P_n^{m'}(\cos\theta)e^{im\phi}, \tag{2.14b}$$

$$H^+_{TE,\phi} = \frac{B_{nm}m}{Z_0r}\left[h_n^{(1)}(k_0r) + k_0rh_n^{(1)'}(k_0r)\right]\frac{P_n^m(\cos\theta)}{\sin\theta}e^{im\phi}. \tag{2.14c}$$

To determine the dispersion relation, there are two boundary conditions applied. $\boldsymbol{E}^-_{TE,\parallel} = \boldsymbol{E}^+_{TE,\parallel}$ gives

$$\left\{kA_{nm}j_n(kr) - k_0B_{nm}h_n^{(1)}(k_0r)\right\}\Big|_{r=R} = 0 \tag{2.15a}$$

and $\boldsymbol{H}^-_{TE,\parallel} = \boldsymbol{H}^+_{TE,\parallel}$ gives

$$\left\{\sqrt{\frac{\varepsilon}{\varepsilon_0}}A_{nm}\frac{\mathrm{d}[krj_n(kr)]}{\mathrm{d}kr} - B_{nm}\frac{\mathrm{d}\left[k_0rh_n^{(1)}(k_0r)\right]}{\mathrm{d}k_0r}\right\}\Big|_{r=R} = 0. \tag{2.15b}$$

To obtain non-zero solutions for A_{nm} and B_{nm}, Eq. (2.15) yields the dispersion relation for TE modes

$$\left\{j_n(kr)\frac{\mathrm{d}\left[k_0rh_n^{(1)}(k_0r)\right]}{\mathrm{d}k_0r} - h_n^{(1)}(k_0r)\frac{\mathrm{d}[krj_n(kr)]}{\mathrm{d}kr}\right\}\Big|_{r=R} = 0 \tag{2.16}$$

Similarly for TM modes, since $H_r = 0$ everywhere, the fields can be described by

$$\boldsymbol{E}^-_{TM} = \frac{iZ}{k}\boldsymbol{\nabla}\times\boldsymbol{H}^-_{TM}, \qquad \boldsymbol{H}^-_{TM} = C_{nm}\boldsymbol{M}^-_{nm}(\boldsymbol{r},k) \qquad \text{for } r<R; \tag{2.17}$$

$$\boldsymbol{E}^+_{TM} = \frac{iZ_0}{k_0}\boldsymbol{\nabla}\times\boldsymbol{H}^+_{TM}, \qquad \boldsymbol{H}^+_{TM} = D_{nm}\boldsymbol{M}^+_{nm}(\boldsymbol{r},k_0) \qquad \text{for } r>R \tag{2.18}$$

doi:10.6342/NTU202300933

where $\boldsymbol{M}^{-}_{nm}(\boldsymbol{r}, k)$ and $\boldsymbol{M}^{+}_{nm}(\boldsymbol{r}, k_0)$ are again given in Eqs. (2.9) and (2.10), and C_{nm}, D_{nm} are some constants. Then the electric field components are given by

$$E^{-}_{TM,r} = \frac{iC_{nm}Zn(n+1)}{r} j_n(kr) P^m_n(\cos\theta) e^{im\phi}, \tag{2.19a}$$

$$E^{-}_{TM,\theta} = -\frac{iC_{nm}Z}{r}[j_n(kr) + krj'_n(kr)] \sin\theta P^{m'}_n(\cos\theta) e^{im\phi}, \tag{2.19b}$$

$$E^{-}_{TM,\phi} = -\frac{C_{nm}Zm}{r}[j_n(kr) + krj'_n(kr)] \frac{P^m_n(\cos\theta)}{\sin\theta} e^{im\phi}; \tag{2.19c}$$

$$E^{+}_{TM,r} = \frac{iD_{nm}Z_0n(n+1)}{r} h^{(1)}_n(k_0r) P^m_n(\cos\theta) e^{im\phi}, \tag{2.20a}$$

$$E^{+}_{TM,\theta} = -\frac{iD_{nm}Z_0}{r}\left[h^{(1)}_n(k_0r) + k_0rh^{(1)'}_n(k_0r)\right] \sin\theta P^{m'}_n(\cos\theta) e^{im\phi}, \tag{2.20b}$$

$$E^{+}_{TM,\phi} = -\frac{D_{nm}Z_0m}{r}\left[h^{(1)}_n(k_0r) + k_0rh^{(1)'}_n(k_0r)\right] \frac{P^m_n(\cos\theta)}{\sin\theta} e^{im\phi}. \tag{2.20c}$$

The magnetic field components are given by

$$H^{-}_{TM,r} = 0, \tag{2.21a}$$

$$H^{-}_{TM,\theta} = iC_{nm}mkj_n(kr) \frac{P^m_n(\cos\theta)}{\sin\theta} e^{im\phi}, \tag{2.21b}$$

$$H^{-}_{TM,\phi} = C_{nm}kj_n(kr) \sin\theta P^{m'}_n(\cos\theta) e^{im\phi}; \tag{2.21c}$$

$$H^{+}_{TM,r} = 0, \tag{2.22a}$$

$$H^{+}_{TM,\theta} = iD_{nm}mk_0h^{(1)}_n(k_0r) \frac{P^m_n(\cos\theta)}{\sin\theta} e^{im\phi}, \tag{2.22b}$$

$$H^{+}_{TM,\phi} = D_{nm}k_0h^{(1)}_n(k_0r) \sin\theta P^{m'}_n(\cos\theta) e^{im\phi}. \tag{2.22c}$$

Hence, applying boundary conditions yields the dispersion relation for TM modes

$$\left\{\frac{\varepsilon}{\varepsilon_0} j_n(kr) \frac{\mathrm{d}\left[k_0rh^{(1)}_n(k_0r)\right]}{\mathrm{d}k_0r} - h^{(1)}_n(k_0r) \frac{\mathrm{d}[krj_n(kr)]}{\mathrm{d}kr}\right\}\Bigg|_{r=R} = 0 \tag{2.23}$$

Combining Eqs. (2.11) – (2.14) and (2.16) gives the analytic solution of the fields for TE modes, while combining Eqs. (2.19) – (2.22) and (2.23) gives the analytic solution of

doi:10.6342/NTU202300933

the fields for TM modes. The modes are denoted by TE_{nmq} or TM_{nmq}, where $n \in \mathbb{N}$ is the mode number, $0 \leq m \leq n$ is the number of azimuthal oscillations, and $q \in \mathbb{N}$ represents the q-th root of the dispersion relation.

2.2 Methods

Python was used to solve for the radius of the dielectric sphere R in Eqs. (2.16) and (2.23) at constant frequency $2.45\,\mathrm{GHz}$, and also to generate the field profile data. The dielectric of interest in this analysis is water, with complex permittivity ε satisfying Debye model. The real part and the imaginary part of $\varepsilon/\varepsilon_0$ are given by the Debye-type relaxation function [2]

$$\varepsilon'(\omega) = \varepsilon(\infty) + \frac{\varepsilon(0) - \varepsilon(\infty)}{1 + \omega^2\tau^2}; \tag{2.24a}$$

$$\varepsilon''(\omega) = \frac{\omega\tau[\varepsilon(0) - \varepsilon(\infty)]}{1 + \omega^2\tau^2} \tag{2.24b}$$

where the parameters in the relations are low-frequency permittivity $\varepsilon(0)$, extrapolated high-frequency permittivity $\varepsilon(\infty)$, and relaxation time τ. Values of these parameters at different temperatures are shown in Table 2.2. In this analysis, the temperature of interest is $25\,^\circ\mathrm{C}$. Fig. 2.1 presents the complex dielectric constant of water at $25\,^\circ\mathrm{C}$ as a function of frequency. Hence, $\varepsilon/\varepsilon_0 = 77.19 + 9.7i$ is used for water in this analysis.

2.3 Results and Discussion

Generally, the field profiles of TE modes and TM modes are different since they satisfy different boundary conditions. However, there are still some common characteristics for each mode. The purpose of this section is to find the field characteristics of numbers in mode notations, i.e., n, m, q, through examining the field profiles of first few modes. The radius of the water sphere for each mode at $2.45\,\mathrm{GHz}$ is shown in Table 2.3. The field amplitude of each mode is normalized for readability and convenience, where the color

doi:10.6342/NTU202300933

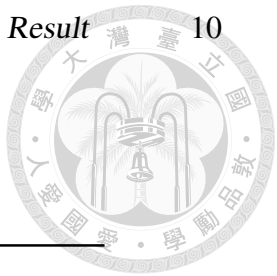

Temperature (°C)	$\varepsilon(0) \pm \Delta\varepsilon(0)$	$\varepsilon(\infty) \pm \Delta\varepsilon(\infty)$	$\tau \pm \Delta\tau$ (ps)
10	83.92± 0.20	5.5± 0.2	12.68± 0.10
15	82.05± 0.20	6.0± 0.5	10.83± 0.20
20	80.21± 0.20	5.6± 0.2	9.36± 0.05
25	78.36± 0.05	5.2± 0.1	8.27± 0.02
30	76.56± 0.20	5.2± 0.4	7.28± 0.05
40	73.18± 0.20	3.9± 0.3	5.82± 0.05
50	69.89± 0.20	4.0± 0.3	4.75± 0.05

Table 2.2: Parameters of Eq. (2.24) at different temperatures [2].

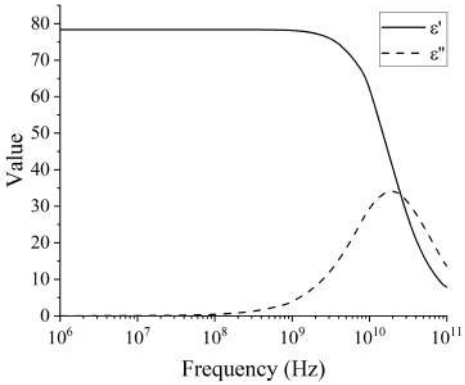

Figure 2.1: The complex dielectric constant of water at 25 °C as a function of frequency.

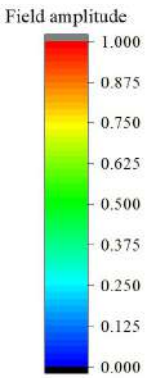

Figure 2.2: The normalized color scale for field profiles in Section 2.3.

doi:10.6342/NTU202300933

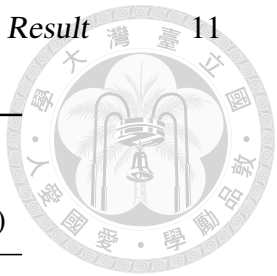

TE modes		TM modes	
Mode	Radius (mm)	Mode	Radius (mm)
TE_{101}	6.88	TM_{101}	9.81
TE_{102}	13.81	TM_{102}	16.86
TE_{103}	20.77	TM_{103}	24.00
TE_{201}	9.91	TM_{201}	12.69
TE_{211}	9.91	TM_{211}	12.69
TE_{221}	9.91	TM_{221}	12.69
TE_{301}	12.74	TM_{301}	15.42

Table 2.3: Water sphere radius at 2.45 GHz for each normal mode.

scale is shown in Fig. 2.2. In practice, the strength of resonance is determined by power source and properties of resonant cavities (e.g., shape, size, material).

Starting from n, the mode number, Fig. 2.3 and 2.4 show the field profiles of TE_{n01} modes, while Fig. 2.5 and 2.6 show the field profiles of TM_{n01} modes. It is obvious that n represents the number of poles, determining the basic profile of the fields. $n = 1$ modes are dipolar modes, $n = 2$ modes are quadrupolar modes, $n = 3$ modes are octupolar modes, and so on.

As for m, the azimuthal oscillation number, Fig. 2.7 and 2.8 show the field profiles of TE_{2m1} modes, while Fig. 2.9 and 2.10 show the field profiles of TM_{2m1} modes. The modes with same n but different m share the same solutions to the dispersion relations, hence having the same pole numbers. m represents the number of azimuthal oscillations, thus giving different ϕ-dependency. To be specific, for $m = 0$, the fields are azimuthally uniform; for $m = n$, the azimuthal field profiles (i.e., those of xy-plane) indicate the respective multipolar modes.

Finally, for q, the root number of the dispersion relation, Fig. 2.11 and 2.12 show the field profiles of TE_{10q} modes, while Fig. 2.13 and 2.14 show the field profiles of TM_{10q}

doi:10.6342/NTU202300933

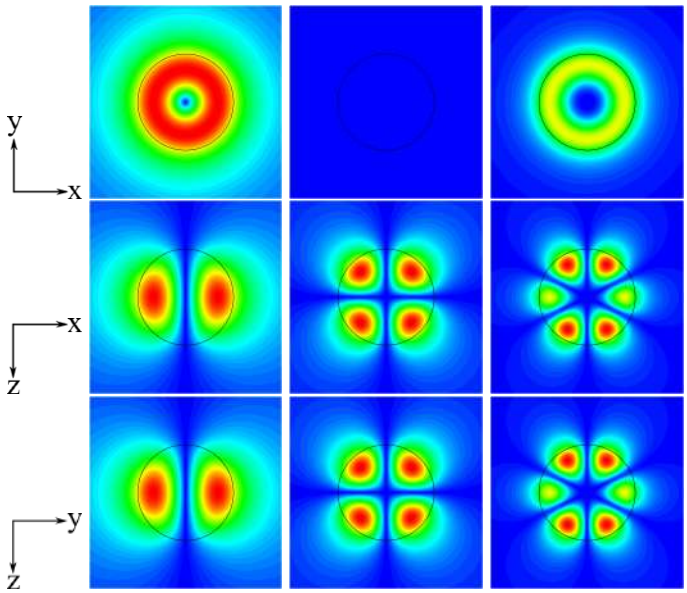

(a) TE_{101} (b) TE_{201} (c) TE_{301}

Figure 2.3: Electric field profiles of TE_{n01} modes.

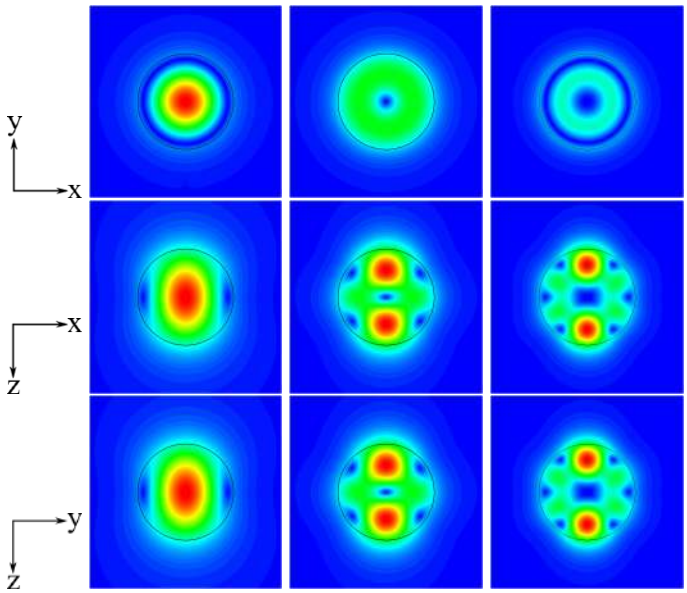

(a) TE_{101} (b) TE_{201} (c) TE_{301}

Figure 2.4: Magnetic field profiles of TE_{n01} modes.

doi:10.6342/NTU202300933

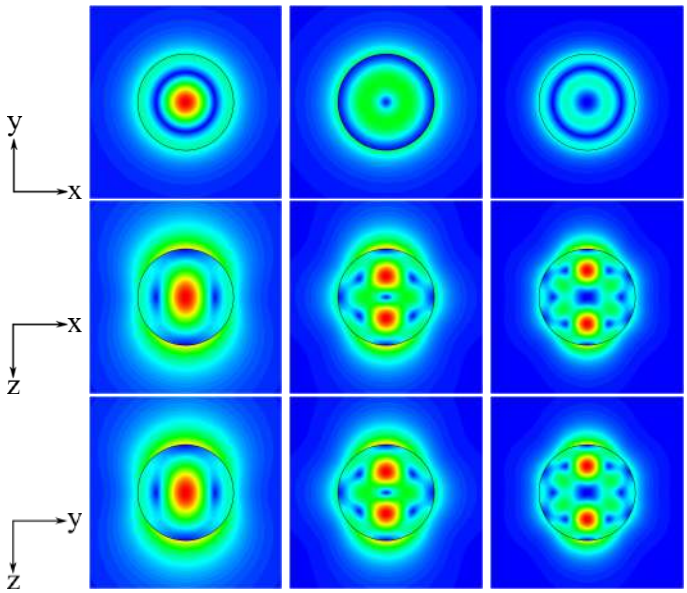

(a) TM_{101} (b) TM_{201} (c) TM_{301}

Figure 2.5: Electric field profiles of TM_{n01} modes.

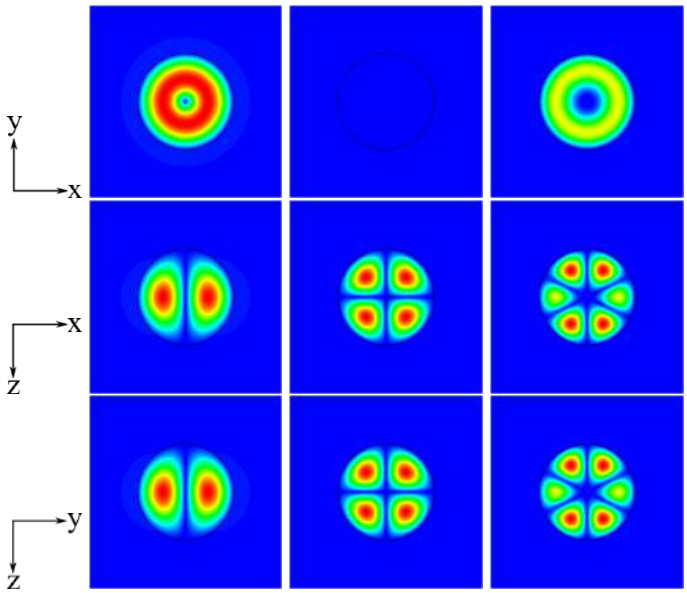

(a) TM_{101} (b) TM_{201} (c) TM_{301}

Figure 2.6: Magnetic field profiles of TM_{n01} modes.

doi:10.6342/NTU202300933

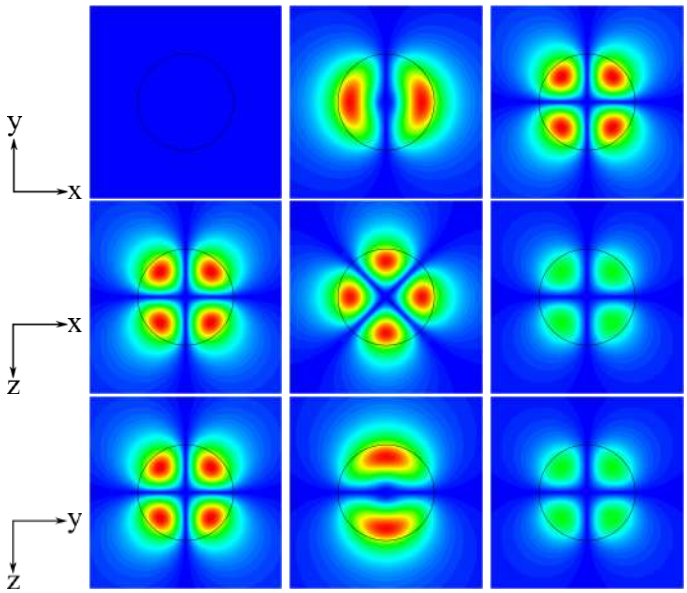

(a) TE_{201} (b) TE_{211} (c) TE_{221}

Figure 2.7: Electric field profiles of TE_{2m1} modes.

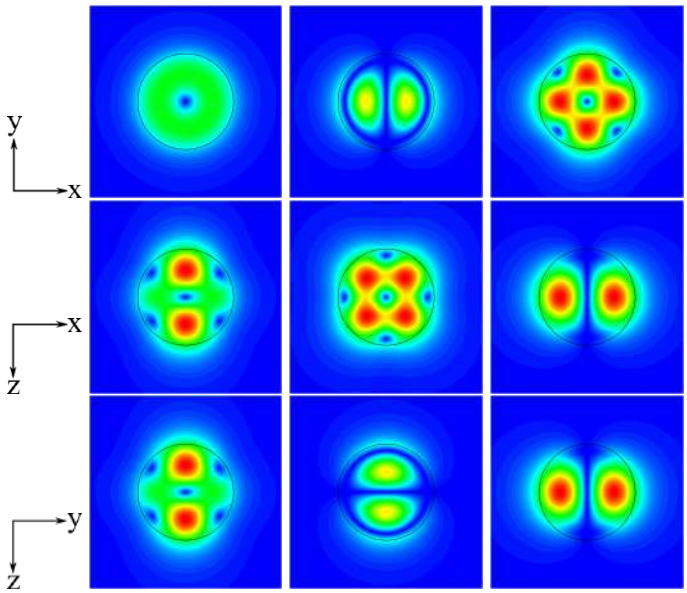

(a) TE_{201} (b) TE_{211} (c) TE_{221}

Figure 2.8: Magnetic field profiles of TE_{2m1} modes.

doi:10.6342/NTU202300933

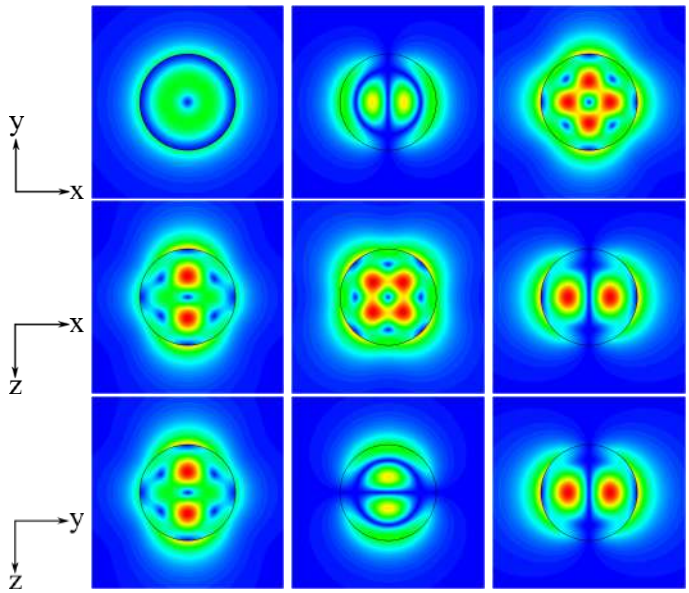

(a) TM_{201} (b) TM_{211} (c) TM_{221}

Figure 2.9: Electric field profiles of TM_{2m1} modes.

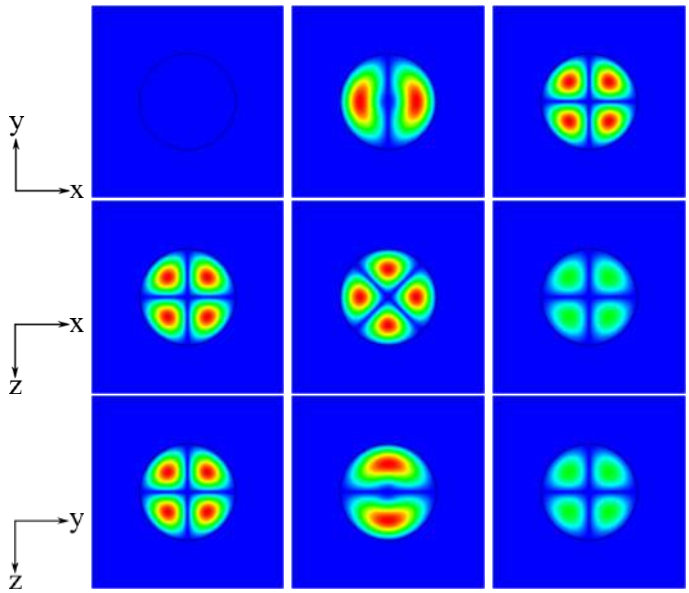

(a) TM_{201} (b) TM_{211} (c) TM_{221}

Figure 2.10: Magnetic field profiles of TM_{2m1} modes.

doi:10.6342/NTU202300933

modes. The modes with same n but different q are derived from same dispersion relations, having the same pole numbers but with larger R. This can be seen in the figures presented. The field profiles with higher q modes are basically the same as those with lower q modes, surrounded by a "shell" with same multipoles. Besides, due to the same m, these modes basically have the same azimuthal dependency.

doi:10.6342/NTU202300933

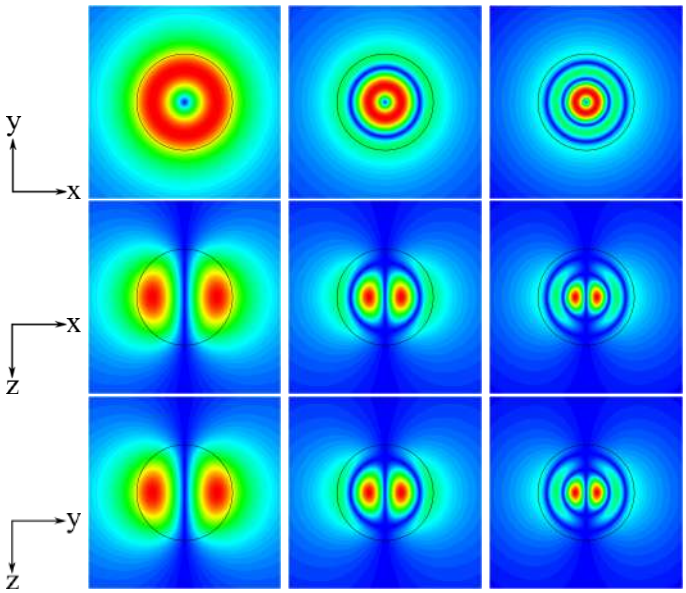

(a) TE_{101} (b) TE_{102} (c) TE_{103}

Figure 2.11: Electric field profiles of TE_{10q} modes.

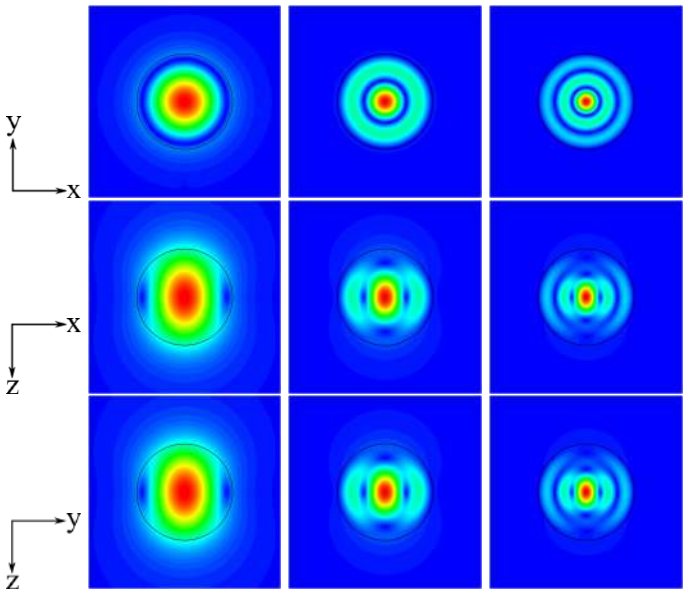

(a) TE_{101} (b) TE_{102} (c) TE_{103}

Figure 2.12: Magnetic field profiles of TE_{10q} modes.

doi:10.6342/NTU202300933

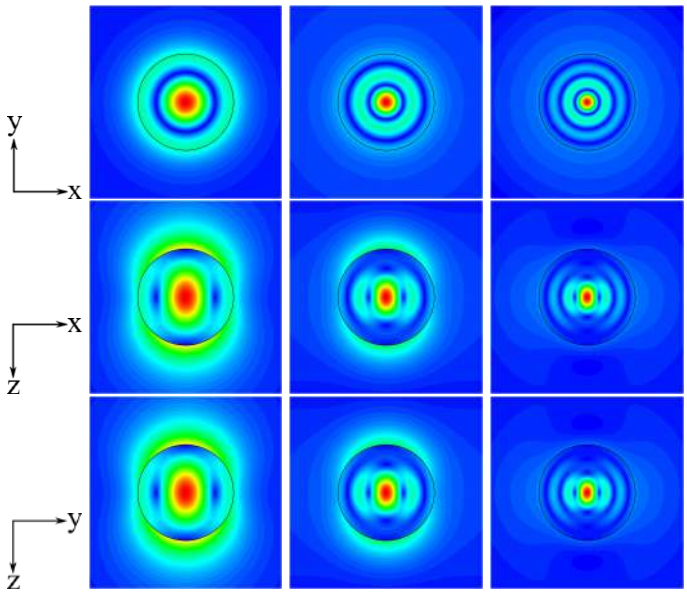

(a) TM_{101} (b) TM_{102} (c) TM_{103}

Figure 2.13: Electric field profiles of TM_{10q} modes.

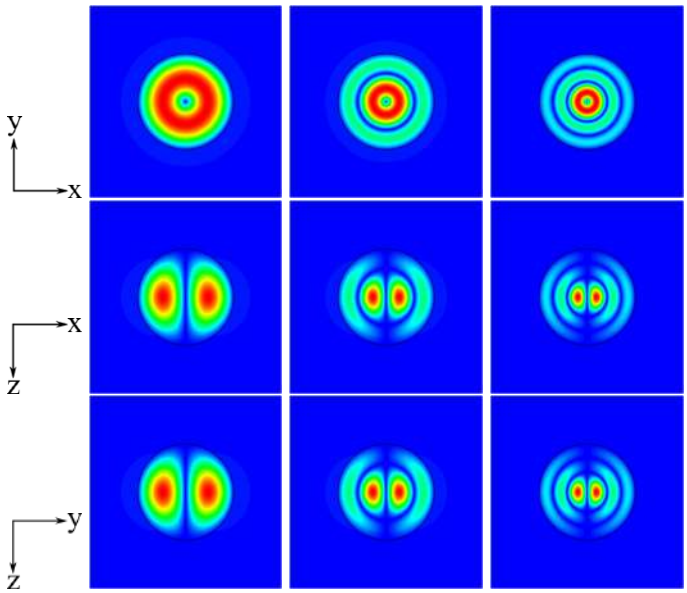

(a) TM_{101} (b) TM_{102} (c) TM_{103}

Figure 2.14: Magnetic field profiles of TM_{10q} modes.

doi:10.6342/NTU202300933

Chapter 3

A Water Sphere Hit by a 2.45 GHz Plane Wave: Analytical Analysis

The main purpose of this chapter is to examine the fields of a water sphere hit by a uniform plane wave, and to compare those with the resonant fields in Chapter 2. What causes the difference between these two? Furthermore, how does the radius of water sphere affect the fields' properties and power absorption rate, and why? In this chapter, Section 3.1 derives the analytic solutions; Section 3.3 answers these questions through analyzing field amplitude, field uniformity, and some representative field profiles.

3.1 Theory

Consider the same dielectric sphere discussed in Section 2.1 hit by a uniform plane wave polarized at x-axis and propagating along z-axis. The total fields can be separated into incident ones and scattered ones, and can also be expressed as the sum of TE modes

doi:10.6342/NTU202300933

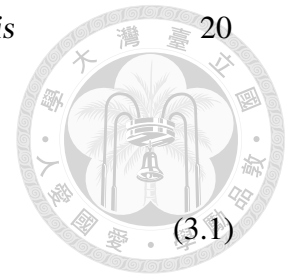

and TM modes, i.e.,

$$\boldsymbol{E} = \boldsymbol{E}^{inc} + \boldsymbol{E}^{sc} = \sum_{n=1}^{\infty} \boldsymbol{E}_n^{TE} + \sum_{n=1}^{\infty} \boldsymbol{E}_n^{TM}; \tag{3.1}$$

$$\boldsymbol{H} = \boldsymbol{H}^{inc} + \boldsymbol{H}^{sc} = \sum_{n=1}^{\infty} \boldsymbol{H}_n^{TE} + \sum_{n=1}^{\infty} \boldsymbol{H}_n^{TM}. \tag{3.2}$$

The scattered fields are simply linear combinations of those generated by a spherical dielectric resonator, including TE modes (Eqs. (2.11) – (2.14)) and TM modes (Eqs. (2.19) – (2.22)). The coefficients of each modes are rearranged to a_n, b_n, c_n, d_n, corresponding to $A_{nm}, B_{nm}, C_{nm}, D_{nm}$. For simplicity and readability, two of the Riccati-Bessel functions [22] are in use later in the field expressions, which are

$$S_n(x) = x j_n(x) \quad \text{and} \quad \xi_n(x) = x h_n^{(1)}(x). \tag{3.3}$$

As for the incident fields, following the assumption $E, H \sim e^{-i\omega t}$, the fields of the incident plane wave can be expressed as

$$\boldsymbol{E}^{inc} = E_0\, e^{ik_0 z}\hat{\boldsymbol{x}} = E_0\, e^{ik_0 r\cos\theta}\hat{\boldsymbol{x}}; \tag{3.4}$$

$$\boldsymbol{H}^{inc} = \frac{E_0}{Z_0}\, e^{ik_0 z}\hat{\boldsymbol{y}} = H_0\, e^{ik_0 r\cos\theta}\hat{\boldsymbol{y}}. \tag{3.5}$$

Harrington [23] shows that a plane wave can be expressed in terms of spherical wave functions through

$$e^{iz} = e^{ir\cos\theta} = \sum_{n=0}^{\infty} i^n (2n+1) j_n(r) P_n(\cos\theta). \tag{3.6}$$

Hence, the r-component of the incident fields are

$$E_r^{inc} = E^{inc}\sin\theta\cos\phi = iE_0\cos\phi \sum_{n=1}^{\infty} e_n n(n+1)\frac{S_n(k_0 r)}{(k_0 r)^2} P_n^1(\cos\theta); \tag{3.7}$$

$$H_r^{inc} = H^{inc}\sin\theta\sin\phi = iH_0\sin\phi \sum_{n=1}^{\infty} e_n n(n+1)\frac{S_n(k_0 r)}{(k_0 r)^2} P_n^1(\cos\theta) \tag{3.8}$$

where

$$e_n = \frac{i^n(2n+1)}{n(n+1)} \tag{3.9}$$

doi:10.6342/NTU202300933

is introduced for convenience and the $n = 0$ terms are dropped since $P_0^1(\cos\theta) = 0$. Eqs. (3.7) and (3.8) can be seen as the r-component of TM modes and TE modes, respectively. Then the other components can be constructed through observing the form and comparing the coefficients in Eqs. (2.11)(2.19) and Eqs. (2.13)(2.21).

Thus, through Eqs. (3.1) and (3.2), the electric field components are

$$E_r^- = iE_0\cos\phi\sum_{n=1}^{\infty} c_n n(n+1)\frac{S_n(kr)}{(kr)^2}P_n^1(\cos\theta), \tag{3.10a}$$

$$\begin{aligned} E_\theta^- = &-E_0\cos\phi\sum_{n=1}^{\infty} a_n\frac{S_n(kr)}{kr}\frac{P_n^1(\cos\theta)}{\sin\theta} \\ &- iE_0\cos\phi\sum_{n=1}^{\infty} c_n\frac{S_n'(kr)}{kr}\sin\theta P_n^{1'}(\cos\theta), \end{aligned} \tag{3.10b}$$

$$\begin{aligned} E_\phi^- = &-E_0\sin\phi\sum_{n=1}^{\infty} a_n\frac{S_n(kr)}{kr}\sin\theta P_n^{1'}(\cos\theta) \\ &- iE_0\sin\phi\sum_{n=1}^{\infty} c_n\frac{S_n'(kr)}{kr}\frac{P_n^1(\cos\theta)}{\sin\theta}; \end{aligned} \tag{3.10c}$$

$$E_r^+ = iE_0\cos\phi\sum_{n=1}^{\infty}\left[d_n\frac{\xi_n(k_0r)}{(k_0r)^2} + e_n\frac{S_n(k_0r)}{(k_0r)^2}\right]n(n+1)P_n^1(\cos\theta), \tag{3.11a}$$

$$\begin{aligned} E_\theta^+ = &-E_0\cos\phi\sum_{n=1}^{\infty}\left[b_n\frac{\xi_n(k_0r)}{k_0r} + e_n\frac{S_n(k_0r)}{k_0r}\right]\frac{P_n^1(\cos\theta)}{\sin\theta} \\ &- iE_0\cos\phi\sum_{n=1}^{\infty}\left[d_n\frac{\xi_n'(k_0r)}{k_0r} + e_n\frac{S_n'(k_0r)}{k_0r}\right]\sin\theta P_n^{1'}(\cos\theta), \end{aligned} \tag{3.11b}$$

$$\begin{aligned} E_\phi^+ = &-E_0\sin\phi\sum_{n=1}^{\infty}\left[b_n\frac{\xi_n(k_0r)}{k_0r} + e_n\frac{S_n(k_0r)}{k_0r}\right]\sin\theta P_n^{1'}(\cos\theta) \\ &- iE_0\sin\phi\sum_{n=1}^{\infty}\left[d_n\frac{\xi_n'(k_0r)}{k_0r} + e_n\frac{S_n'(k_0r)}{k_0r}\right]\frac{P_n^1(\cos\theta)}{\sin\theta}. \end{aligned} \tag{3.11c}$$

doi:10.6342/NTU202300933

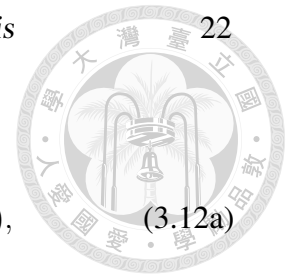

The magnetic field components are

$$H_r^- = i\sqrt{\frac{\varepsilon}{\varepsilon_0}}H_0 \sin\phi \sum_{n=1}^{\infty} a_n n(n+1)\frac{S_n(kr)}{(kr)^2}P_n^1(\cos\theta), \tag{3.12a}$$

$$H_\theta^- = -\sqrt{\frac{\varepsilon}{\varepsilon_0}}H_0 \sin\phi \sum_{n=1}^{\infty} c_n \frac{S_n(kr)}{kr}\frac{P_n^1(\cos\theta)}{\sin\theta} - i\sqrt{\frac{\varepsilon}{\varepsilon_0}}H_0 \sin\phi \sum_{n=1}^{\infty} a_n \frac{S_n'(kr)}{kr}\sin\theta P_n^{1'}(\cos\theta), \tag{3.12b}$$

$$H_\phi^- = -\sqrt{\frac{\varepsilon}{\varepsilon_0}}H_0 \cos\phi \sum_{n=1}^{\infty} c_n \frac{S_n(kr)}{kr}\sin\theta P_n^{1'}(\cos\theta) - i\sqrt{\frac{\varepsilon}{\varepsilon_0}}H_0 \cos\phi \sum_{n=1}^{\infty} a_n \frac{S_n'(kr)}{kr}\frac{P_n^1(\cos\theta)}{\sin\theta}; \tag{3.12c}$$

$$H_r^+ = i\sqrt{\frac{\varepsilon}{\varepsilon_0}}H_0 \sin\phi \sum_{n=1}^{\infty}\left[b_n\frac{\xi_n(k_0r)}{(k_0r)^2} + e_n\frac{S_n(k_0r)}{(k_0r)^2}\right]n(n+1)P_n^1(\cos\theta), \tag{3.13a}$$

$$H_\theta^+ = -\sqrt{\frac{\varepsilon}{\varepsilon_0}}H_0 \sin\phi \sum_{n=1}^{\infty}\left[d_n\frac{\xi_n(k_0r)}{k_0r} + e_n\frac{S_n(k_0r)}{k_0r}\right]\frac{P_n^1(\cos\theta)}{\sin\theta} - i\sqrt{\frac{\varepsilon}{\varepsilon_0}}H_0 \sin\phi \sum_{n=1}^{\infty}\left[b_n\frac{\xi_n'(k_0r)}{k_0r} + e_n\frac{S_n'(k_0r)}{k_0r}\right]\sin\theta P_n^{1'}(\cos\theta), \tag{3.13b}$$

$$H_\phi^+ = -\sqrt{\frac{\varepsilon}{\varepsilon_0}}H_0 \cos\phi \sum_{n=1}^{\infty}\left[d_n\frac{\xi_n(k_0r)}{k_0r} + e_n\frac{S_n(k_0r)}{k_0r}\right]\sin\theta P_n^{1'}(\cos\theta) - i\sqrt{\frac{\varepsilon}{\varepsilon_0}}H_0 \cos\phi \sum_{n=1}^{\infty}\left[b_n\frac{\xi_n'(k_0r)}{k_0r} + e_n\frac{S_n'(k_0r)}{k_0r}\right]\frac{P_n^1(\cos\theta)}{\sin\theta}. \tag{3.13c}$$

Applying boundary conditions $\boldsymbol{E}^- = \boldsymbol{E}^+$ and $\boldsymbol{H}^- = \boldsymbol{H}^+$, the coeffieicents are

$$a_n = \frac{\sqrt{\varepsilon/\varepsilon_0}\,S_n'(k_0R)\xi_n(k_0R) - \sqrt{\varepsilon/\varepsilon_0}\,S_n(k_0R)\xi_n'(k_0R)}{\sqrt{\varepsilon/\varepsilon_0}\,S_n'(kR)\xi_n(k_0R) - S_n(kR)\xi_n'(k_0R)}e_n, \tag{3.14a}$$

$$b_n = \frac{-\sqrt{\varepsilon/\varepsilon_0}\,S_n(k_0R)S_n'(kR) + S_n'(k_0R)S_n(kR)}{\sqrt{\varepsilon/\varepsilon_0}\,\xi_n(k_0R)S_n'(kR) - \xi_n'(k_0R)S_n(kR)}e_n, \tag{3.14b}$$

$$c_n = \frac{\sqrt{\varepsilon/\varepsilon_0}\,S_n(k_0R)\xi_n'(k_0R) - \sqrt{\varepsilon/\varepsilon_0}\,S_n'(k_0R)\xi_n(k_0R)}{\sqrt{\varepsilon/\varepsilon_0}\,S_n(kR)\xi_n'(k_0R) - S_n'(kR)\xi_n(k_0R)}e_n, \tag{3.14c}$$

$$d_n = \frac{-\sqrt{\varepsilon/\varepsilon_0}\,S_n'(k_0R)S_n(kR) + S_n(k_0R)S_n'(kR)}{\sqrt{\varepsilon/\varepsilon_0}\,\xi_n'(k_0R)S_n(kR) - \xi_n(k_0R)S_n'(kR)}e_n \tag{3.14d}$$

with e_n introduced in Eq. (3.9). The field expressions are equivalent as shown by Harrington [23], with i replaced by $-i$ due to the assumption $E, H \sim e^{-i\omega t}$.

doi:10.6342/NTU202300933

The time-averaged power per unit volume deposited into the medium is given by [24]

$$P_{loss}(\boldsymbol{x}) = \frac{1}{2}\omega \operatorname{Im}(\varepsilon)|\boldsymbol{E}(\boldsymbol{x})|^2 = \frac{1}{2}\omega \operatorname{Im}(\varepsilon)A(\boldsymbol{x})|E_0|^2 \tag{3.15}$$

where $A(\boldsymbol{x})$ is the local power absorption rate factor defined as

$$A(\boldsymbol{x}) = \frac{|\boldsymbol{E}(\boldsymbol{x})|^2}{|E_0|^2}. \tag{3.16}$$

3.2 Methods

Field profiles were obtained through the same process as in Chapter 2. As for the power absorption rate, given ω, ε, E_0, the power absorption rate is determined by $A(\boldsymbol{x})$ through Eq. (3.15). Then the total absorbed power and field uniformity can be studied through examining the mean power absorption rate factor $\overline{A}$ and its standard deviation σ_A, which are defined as

$$\overline{A} = \frac{\iiint_V A(\boldsymbol{x})\,\mathrm{d}^3x}{\text{Volume}}; \tag{3.17}$$

$$\sigma_A = \sqrt{\frac{\iiint_V \left[A(\boldsymbol{x}) - \overline{A}\right]^2 \mathrm{d}^3x}{\text{Volume}}}. \tag{3.18}$$

The integrals were numerical calculated with Python in spherical coordinates using Simpson's rule [25].

3.3 Results and Discussion

In this section, the comparison between resonant fields and fields with the presence of a uniform plane wave is discussed first. Then, for all water sphere radii, which can be generally divided into three regimes, the dependency of the field properties and the physical reasons behind them are revealed.

doi:10.6342/NTU202300933

3.3.1 Field Analysis: Comparison with Normal Mode

Consider a water sphere of radius $6.8\,\mathrm{mm}$ hit by a $2.45\,\mathrm{GHz}$ uniform plane wave, where its electric field profiles on three planes are shown in Fig. 3.1a. As a electromagnetic wave hit a dielectric, the wave power will be partially absorbed, weakening the field strength along the propagating axis (in this case, z-axis). Other than that, there are two primary effects determining the field patterns, *Resonance* and *Polarization Charge Shielding Effect*.

Firstly, Table 2.3 shows that the predominant resonant mode in this case is TE_{101}, where its electric field profiles are shown in Fig. 3.1b. Note that the orientation has been adjusted to correspond to Fig. 3.1a, and the field amplitude has been rescaled for comparability. Observing Fig. 3.1a and Fig. 3.1b, the field profiles inside the sphere are highly similar, while those outside the sphere have a great difference.

Secondly, Jackson [26] and Chu [27] give a clear explanation for the polarization charge shielding effect. With the presence of an external electric field, the bound molecular charges in a dielectric medium will be slightly displaced to form polarization charges, partially cancelling the external electric field in the dielectric medium while strengthening the electric field on the outside. In particular, consider a uniform dielectric sphere in a uniform and static external electric field $\boldsymbol{E}_{ext} = E_0\hat{\boldsymbol{x}}$. The surface polarization charges σ_{pol} are given by [26]

$$\sigma_{pol} = 3\,\varepsilon_0\left(\frac{\varepsilon/\varepsilon_0 - 1}{\varepsilon/\varepsilon_0 + 2}\right)\boldsymbol{E}_{ext}\cdot\hat{\boldsymbol{r}}. \tag{3.19}$$

Fig. 3.1c shows the total electric field profiles, where the interior electric field $\boldsymbol{E}_{in}$ and exterior electric field $\boldsymbol{E}_{out}$ are obtained analytically through

$$\boldsymbol{E}_{in} = \frac{3}{\varepsilon/\varepsilon_0 + 2}\boldsymbol{E}_{ext}, \tag{3.20a}$$

$$\boldsymbol{E}_{out} = \boldsymbol{E}_{ext} + \frac{3\hat{\boldsymbol{r}}(\boldsymbol{p}\cdot\hat{\boldsymbol{r}}) - \boldsymbol{p}}{4\pi\varepsilon_0 r^3} \tag{3.20b}$$

with $\boldsymbol{p}$ being the total dipole moment. Eq. (3.19) indicates that the electric field generated from polarization charges is stronger along $\boldsymbol{E}_{ext}$, which agrees with Fig. 3.1a that the exterior electric field is enhanced along x-axis. Indeed, observing Fig. 3.1a and Fig. 3.1c,

doi:10.6342/NTU202300933

the exterior electric field along x-axis are highly similar.

Summing up, in the case that a water sphere of radius $6.8\,\mathrm{mm}$ hit by a $2.45\,\mathrm{GHz}$ uniform plane wave, the electric field pattern is a result of combined resonance and polarization charge shielding effect. The interior field is mainly determined by resonance, whereas the polarization charge effect takes a significant part when it comes to the exterior field.

3.3.2 Field Analysis: General Dependency on Water Sphere Radius

Generally, $\overline{A}$ and σ_A are highly dependent on the radius of water sphere as demonstrated in Fig. 3.2. This trend can be separated into three regimes, with the representative field profiles shown in Fig. 3.3 and Fig. 3.4.

1. Regime I: $R \ll \lambda_{water}$

   It is well known that the wavelength of an electromagnetic wave is shortened inside a dielectric medium, which is given by [12]

   $$\lambda_d = \frac{\lambda_0}{\sqrt{\varepsilon/\varepsilon_0}} \tag{3.21}$$

   where λ_0 is the wavelength in free space. Thus, in the presented case, $\lambda_0 = 122.4\,\mathrm{mm}$ and $\lambda_{water} = 13.9\,\mathrm{mm}$. In this regime, the quasi-static limit is satisfied. In this limit, the resonant frequency is high above the frequency of the incident wave. Hence, only polarization charge shielding effect takes presence. The fields are then well approximated by those of the static case through Eq. (3.20), which gives

   $$|\boldsymbol{E}_{in}| \approx 0.038 \quad \text{and} \quad \overline{A} \approx 0.0014. \tag{3.22}$$

   Fig. 3.2, Fig. 3.3a, and Fig. 3.4a are in good agreement with Eq. (3.22), that $\overline{A} \to 0.0014$ and negligible σ_A as $R \to 0$.

2. Regime II: $\lambda_{water}/2 < R < \delta$

   In this regime, with the dimension of the water sphere exceeding the condition

doi:10.6342/NTU202300933

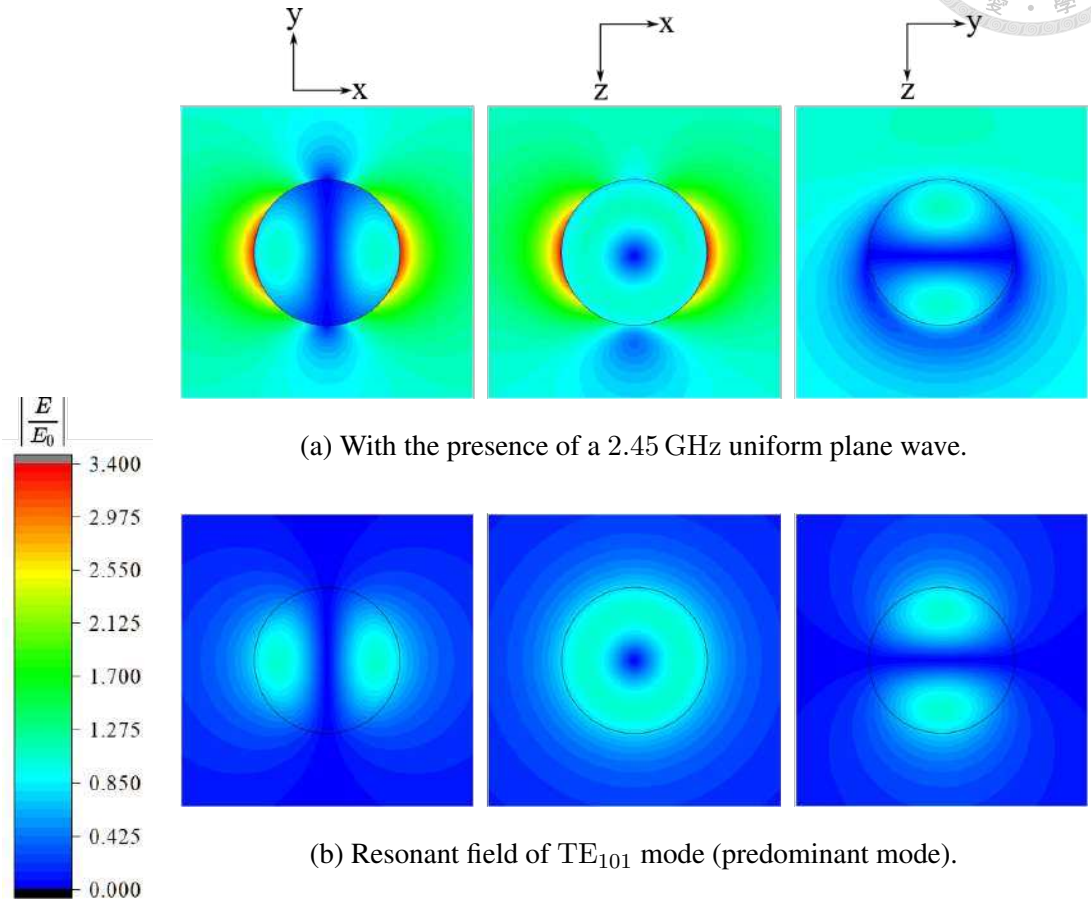

(a) With the presence of a 2.45 GHz uniform plane wave.

(b) Resonant field of TE_{101} mode (predominant mode).

(c) In a uniform and static external electric field.

Figure 3.1: Electric field profiles for a water sphere of radius 6.8 mm in three circumstances.

doi:10.6342/NTU202300933

for quasi-static limit, the water sphere behaves as a spherical resonator. Table 2.3 shows that TE_{101} mode is the predominant resonant mode at $R = 6.8\,\mathrm{mm}$, whose field profiles are shown in Fig. 3.3b and Fig. 3.4b. The second one, TM_{101} mode, is predominant at $R = 9.8\,\mathrm{mm}$, whose field profiles are shown in Fig. 3.3c and Fig. 3.4c. It is clear that polarization charge shielding effect still takes a significant part on the sphere exterior, while the resonance dominates the sphere interior. In Fig. 3.2, $\overline{A}$ and σ_A vary dramatically with respect to R in regime II, which also indicates the dominating behavior of resonances inside the sphere.

3. Regime III: $R > \delta$

   The power of the incident wave attenuates exponentially as penetrating into a medium, and drops to $1/e$ as the incident wave penetrates beyond skin depth δ, which is given by [12]

$$\delta = \frac{1}{2\,\mathrm{Im}\sqrt{\mu\varepsilon}\,\omega} \approx 17.2\,\mathrm{mm} \text{ for water at } 2.45\,\mathrm{GHz}. \tag{3.23}$$

   Hence, as R increases beyond skin depth, $\overline{A}$ drops as in Fig. 3.2a. Besides, a greater dielectric sphere allows several high-order resonant modes to exist at once. These modes overlap to form smoother field patterns as in Fig. 3.3d and Fig. 3.4d, leading to a drop of σ_A in Fig. 3.2b.

In conclusion, $\overline{A}$ and σ_A vary by orders of magnitude over R from $0.1\,\mathrm{mm}$ to $100\,\mathrm{mm}$. This is because that the field pattern is determined by polarization charge shielding effect, resonances, and attenuated incident power, which have high dependency on the dimension of the water sphere.

doi:10.6342/NTU202300933

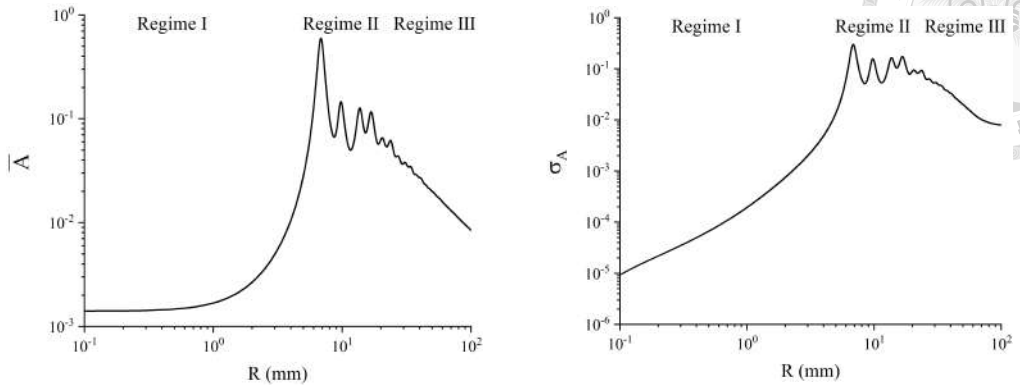

(a) $\overline{A}$ as a function of R. (b) σ_A as a function of R.

Figure 3.2: $\overline{A}$ and σ_A as functions of R showing the behavior of both in three regimes.

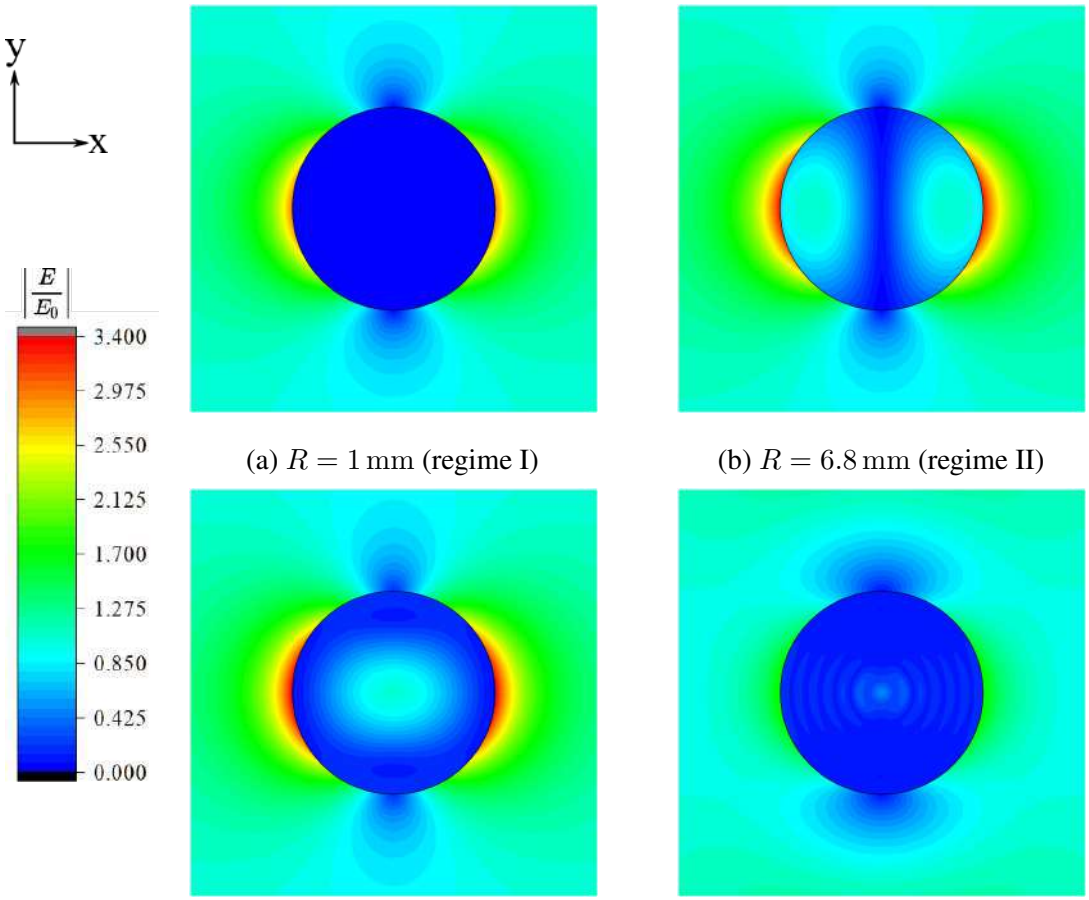

(a) $R = 1\,\mathrm{mm}$ (regime I) (b) $R = 6.8\,\mathrm{mm}$ (regime II)

(c) $R = 9.8\,\mathrm{mm}$ (regime II) (d) $R = 50\,\mathrm{mm}$ (regime III)

Figure 3.3: Electric field profiles on the xy-plane for a water sphere of four radii hit by a $2.45\,\mathrm{GHz}$ uniform plane wave.

doi:10.6342/NTU202300933

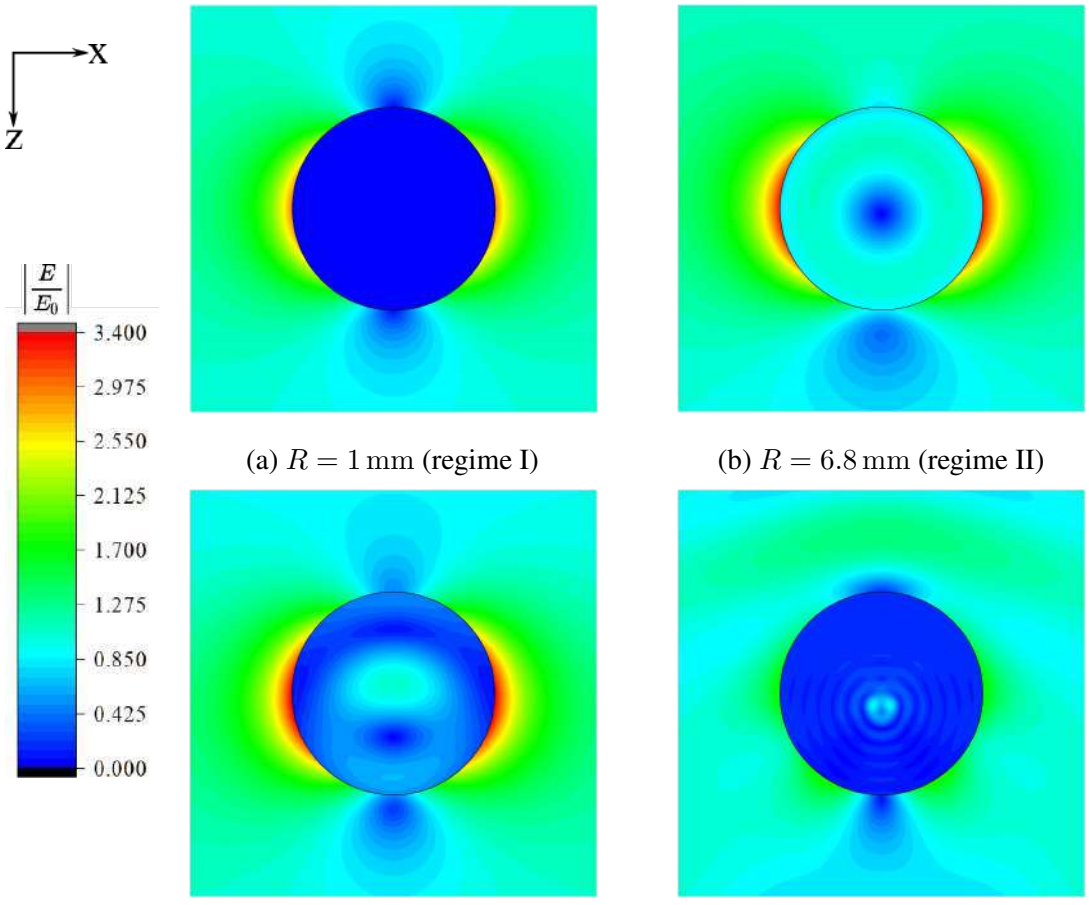

(a) $R = 1\,\mathrm{mm}$ (regime I)

(b) $R = 6.8\,\mathrm{mm}$ (regime II)

(c) $R = 9.8\,\mathrm{mm}$ (regime II)

(d) $R = 50\,\mathrm{mm}$ (regime III)

Figure 3.4: Electric field profiles on the xz-plane for a water sphere of four radii hit by a $2.45\,\mathrm{GHz}$ uniform plane wave.

doi:10.6342/NTU202300933

Chapter 4

Gap Fields between Water Dimers Hit by Plane Waves

In Chapter 3, the properties of the resonance and polarization charge shielding effect for a water sphere are clear. In this chapter, the subject under study has been expanded from single water sphere to water dimer. How do the interior and exterior fields differ from those of single water sphere? How do resonant fields in two spheres affect each other? How do polarization charge shielding effects from two spheres affect each other? Lin *et al.* 's study [1] for water dimers with $\varepsilon/\varepsilon_0 = 78.4 + 0.1i$ at $27\,\mathrm{MHz}$ and $\varepsilon/\varepsilon_0 = 77.5 + 10i$ at $2.45\,\mathrm{GHz}$ can answer these questions.

Lin *et al.* 's study [1] aims to give a detailed physical explanation to a interesting phenomenon, sparks between two closely spaced grapes in a microwave oven. This phenomenon was first scientifically discussed by Khattak [28]. Khattak states that the sparks are caused by a electromagnetic hot spot in the gap of the water dimer, resulting from the merging of resonant modes in two spheres. However, Lin *et al.* [1] give a different explanation. There are three topics discussed, which are a dielectric sphere in a uniform static electric field, a water dimer hit by a $27\,\mathrm{MHz}$ uniform plane wave, and a water dimer hit by a $2.45\,\mathrm{GHz}$ uniform plane wave.

The model of interest is displayed in Fig. 4.1 with incident field amplitude $E_{ext} =$

doi:10.6342/NTU202300933

$400\,\mathrm{V/cm}$. The incident wave is propagating along z-axis and polarized at x-axis. The dimer of interest is aligned parallel to $\boldsymbol{E}_{ext}$.

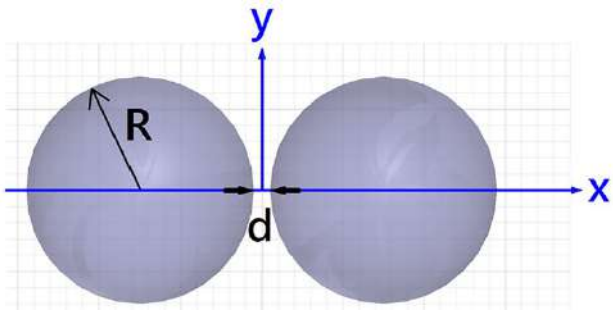

Figure 4.1: Simulation model of a water dimer composed of two water spheres with $R = 7\,\mathrm{mm}$ separated by a variable gap width d, based on Lin *et al.* [1], Fig. 2a.

The first topic, a dielectric sphere in a uniform static electric field, has been discussed in Section 3.3.1. Most importantly, according to Eq. (3.19), the induced polarization charges are greater along $\boldsymbol{E}_{ext}$, and weaker on the sides perpendicular to $\boldsymbol{E}_{ext}$. When the subject in a uniform static electric field is a dimer aligned along $\boldsymbol{E}_{ext}$ as in Fig. 4.1, the induced polarization charges on opposite sides of the gap are of opposite signs. Consequently, more molecules are polarized on both sides, leading to a greater enhancement and thus a stronger electric field in the gap. Moreover, the smaller the gap size is, the greater the enhancment is. This is a well-recognized effect. The question of interest becomes whether the enhancement is strong enough to drive up an air breakdown field in the gap.

In the $27\,\mathrm{MHz}$ case, the water dimer has a dielectric constant $\varepsilon/\varepsilon_0 = 78.4{+}0.1i$, and the wavelength of the electromagnetic wave inside the water dimer $\lambda_{water} \approx 1240\,\mathrm{mm} \gg R$. Thus the fields are quasi-static, and there are no resonances in the dimer. In Fig. 4.2a, the simulation result (with gap width $d = 0.5\,\mathrm{mm}$) shows that the gap field is greatly stronger than E_{ext}, even in the absence of resonance. This suggests that the gap field enhancement is caused by polarization charge shielding effect, where the induced charges are at maximum along $\boldsymbol{E}_{ext}$. For comparison, Fig. 4.2b is the simulation result for the same dimer aligned perpendicular to $\boldsymbol{E}_{ext}$. In this case, the induced charges on both sides of the gap are at

doi:10.6342/NTU202300933

minimum, causing no enhancement of the gap field.

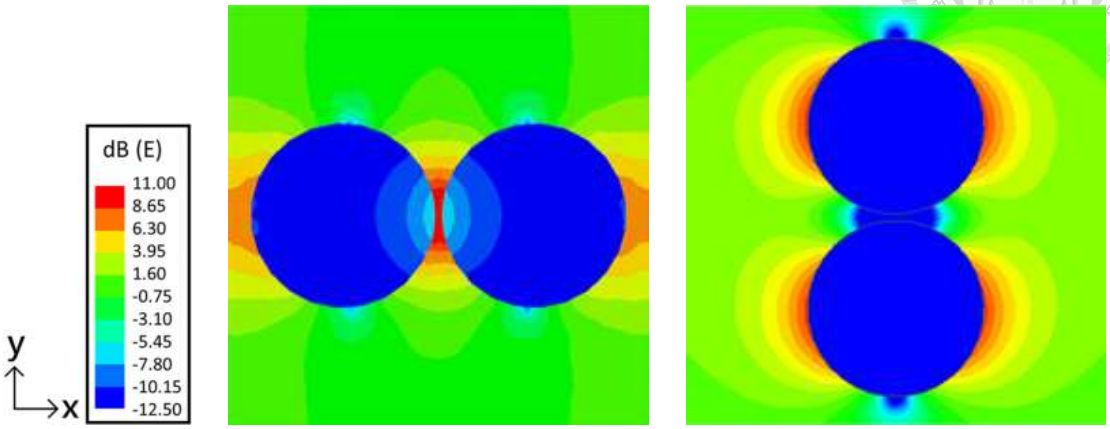

(a) The simulation result with the water dimer aligned along x-axis.

(b) The simulation result with the water dimer aligned along y-axis.

Figure 4.2: Simulation results at $27\,\mathrm{MHz}$ polarized at x-axis under $E_{ext} = 400\,\mathrm{V/cm}$ for different dimer orientations (both with $d = 0.5\,\mathrm{mm}$), based on Lin *et al.* [1], Fig. 2c and Fig. 2g.

Moreover, Fig. 4.3a displays E_{axis} profiles for four values of d, where E_{axis} is the on-axis electric field amplitude along x-axis. It is clear that for all profiles, E_{axis} in the gap region is much stronger than E_{ext}, and smaller d gives a sharper peak of E_{axis} in the gap region. The size of the gap strongly influences the gap field strength, which can be seen in Fig. 4.3b, where $E_{gap} = E_{axis}(x = 0)$. In Fig. 4.3b, gap field strength reaches the air breakdown strength ($\sim 3 \times 10^4\,\mathrm{V/cm}$) at $d \approx 0.13\,\mathrm{mm}$, which suggests that spraks can be ignited with $d \lesssim 0.13\,\mathrm{mm}$.

The explanation of polarization charge enhancement is also supported by the experiment. The experiment was performed using a $27\,\mathrm{MHz}$ capacitor with $E_{ext} = 400\,\mathrm{V/cm}$. The thermal images of the dimer surface after a $35\,\mathrm{s}$-exposure are displayed in Fig. 4.4. Fig. 4.4a shows that the closer the spheres are, the higher the gap surface temperatures are. Besides, Fig. 4.4b shows that the gap-sides of both spheres are not heated even with $d = 0$, suggesting that there is no enhancement in the gap region.

doi:10.6342/NTU202300933

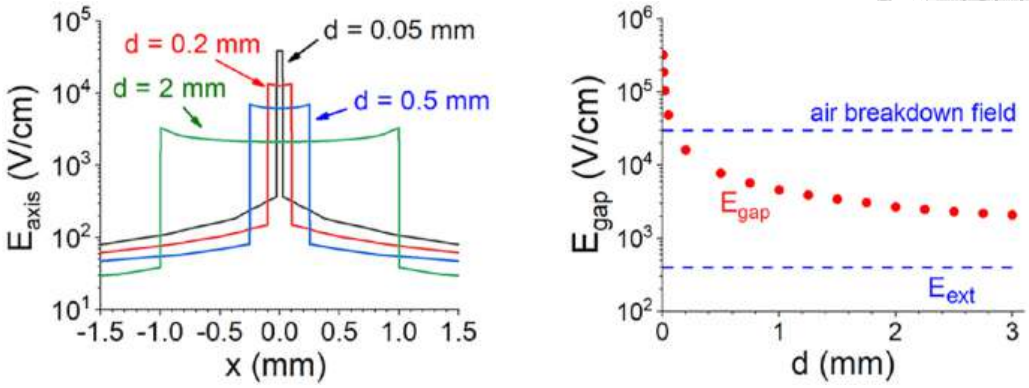

(a) E_{axis} profiles along x-axis for several values of d.

(b) E_{gap} as a function of d.

Figure 4.3: Simulation results at $27\,\mathrm{MHz}$ polarized at x-axis under $E_{ext} = 400\,\mathrm{V/cm}$ for different gap widths d, based on Lin *et al*. [1], Fig. 2d and Fig. 2e.

As for the $2.45\,\mathrm{GHz}$ case, the water dimer has a dielectric constant $\varepsilon/\varepsilon_0 = 77.5 + 10i$. According to Table 2.3 (though with a slightly different $\varepsilon/\varepsilon_0$), a water sphere of $R = 7\,\mathrm{mm}$ works as a strong resonator at $2.45\,\mathrm{GHz}$. As expected, Fig. 4.5 shows that there is a resonant mode in each sphere. Compared with Fig. 3.1a, the interior electric field pattern in Fig. 4.5a has no observable change. Thus, the resonance in each sphere is an independent electromagnetic phenomenon. There is no evidence showing that the resonant modes couple with each other, leading to an electromagnetic hot spot in the gap. Observing the magnetic field pattern in Fig. 4.5b also supports the statement. The gap magnetic field remains weak as gap width d narrows, showing that the effect of resonances is not enhanced in the gap region. In contrast, as shown in Fig. 4.5a, the gap electric field rises significantly as gap width d narrows. This is caused by the polarization charge shielding effect, just as in previous case.

Experiment was also performed for $2.45\,\mathrm{GHz}$ using an antenna with $E_{ext} = 100\,\mathrm{V/cm}$. The thermal images of the dimer after a $10\,\mathrm{s}$-exposure are displayed in Fig. 4.6. The results also support the polarization charge enhancement theory, that the gap surface has a higher temperature as gap width gets narrower in Fig. 4.6a, and there are no temperature rise

doi:10.6342/NTU202300933

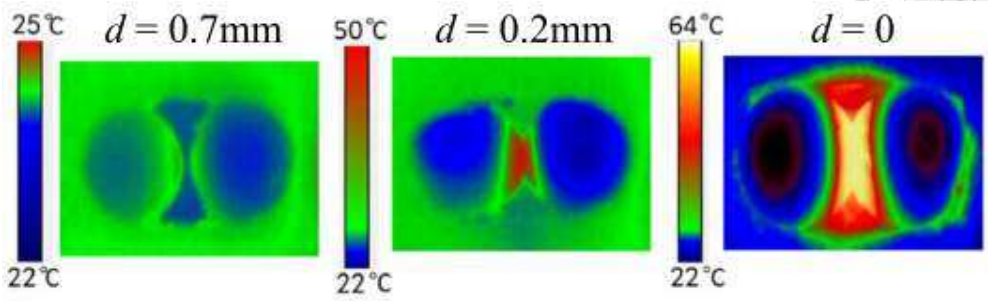

(a) Thermal images of the surface of two $R = 7\,\mathrm{mm}$ hydrogel spheres aligned parallel to the electric field of the capacitor.

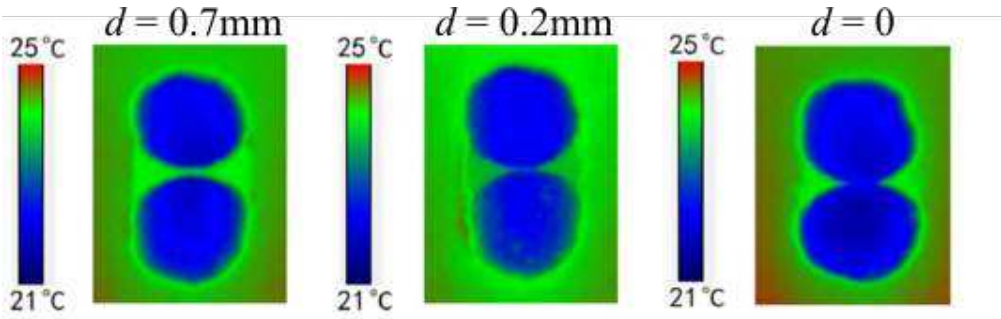

(b) Thermal images of the surface of two $R = 7\,\mathrm{mm}$ hydrogel spheres aligned perpendicular to the electric field of the capacitor.

Figure 4.4: Experiment results of the hydrogel dimer with three values of gap width d in a $27\,\mathrm{MHz}$ capacitor, where $E_{ext} = 400\,\mathrm{V/cm}$ and the exposure time is $35\,\mathrm{s}$, based on Lin *et al.* [1], Fig. 3b and Fig. 3d.

observed when the dimer is aligned perpendicular to $\boldsymbol{E}_{ext}$ in Fig. 4.6b. Note that due to insufficient magnetron power of the antenna, no sparks have been observed.

The enhancement in the gap region of the dimer at $27\,\mathrm{MHz}$ proves the electrical origin for the sparking phenomenon. Even with the presence of resonances as in the $2.45\,\mathrm{GHz}$ case, the polarization charge shielding effect still dominates over the resonant effect in the gap region. More generally, for $\varepsilon/\varepsilon_0 = 77.5 + 10i$, Fig. 4.7 displays the gap field amplitudes as functions of frequency from $10\,\mathrm{MHz}$ to $10\,\mathrm{GHz}$, where $E_{gap} = E_{axis}(x = 0)$ and $H_{gap} = H_{axis}(x = 0)$. Note that Fig. 4.7a is in *log* scale and Fig. 4.7b is in *linear*

doi:10.6342/NTU202300933

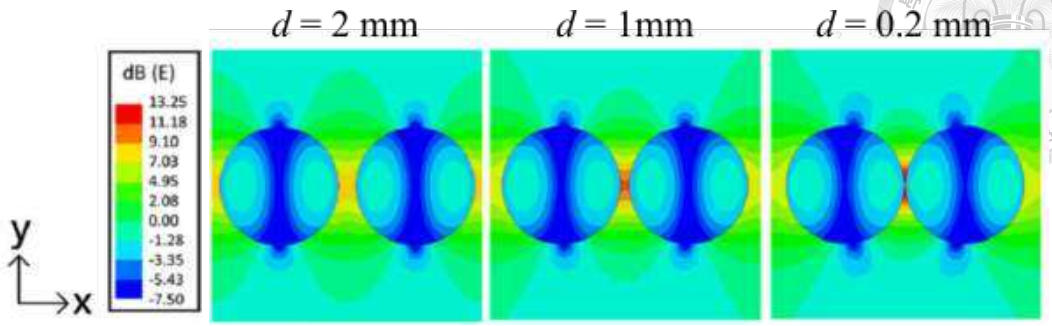

(a) Simulated gap electric field amplitude pattern.

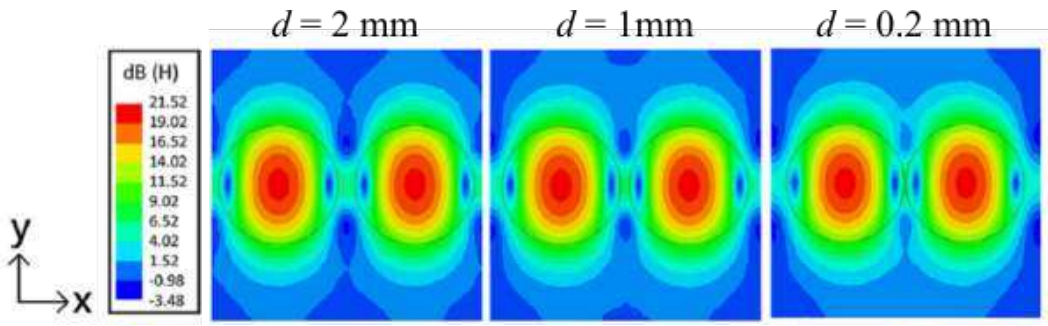

(b) Simulated gap magnetic field amplitude pattern.

Figure 4.5: Simulation results of a water dimer with three gap distances d at $2.45\,\mathrm{GHz}$ polarized at x-axis under $E_{ext} = 400\,\mathrm{V/cm}$, based on Lin *et al.* [1], Fig. 6b and Fig. 6c.

scale. Over the range of interest, Fig. 4.7b demonstrates that the gap magnetic field is barely influenced by the gap distance. Compared to E_{gap}/E_{ext}, H_{gap}/H_{ext} shows the smallness and fluctuating behavior of the fringe fields of the resonances. Moreover, it can be observed in Fig. 4.7a that the gap electric field is independent of f at low frequencies ($< 3\,\mathrm{GHz}$), again suggesting that the polarization charge shielding effect dominates over resonant effect.

To be conclusive, Lin *et al.* [1] give a convincing explanation to the gap-sparking phenomenon in water dimers, which is not caused by the merging of resonances in two spheres but the polarization charge shielding effect. This is also evidenced by simulation and experimental results.

doi:10.6342/NTU202300933

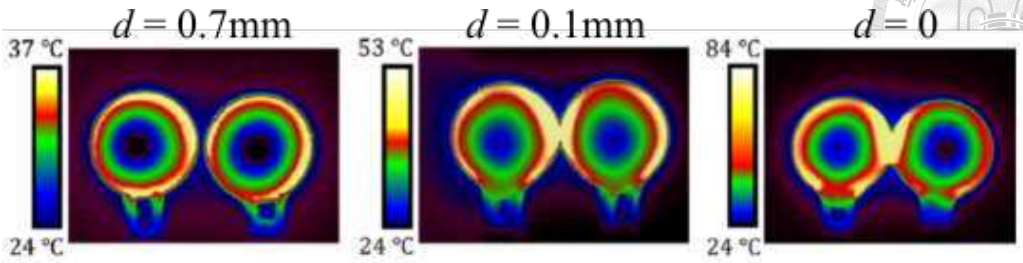

(a) Thermal images of the surface of two $R = 7\,\mathrm{mm}$ hydrogel spheres aligned parallel to $\boldsymbol{E}_{ext}$.

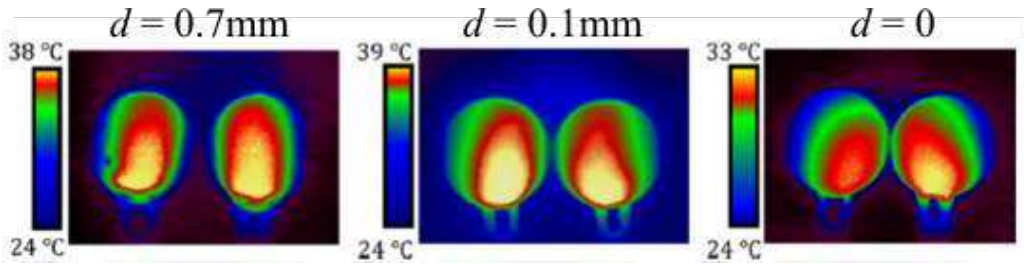

(b) Thermal images of the surface of two $R = 7\,\mathrm{mm}$ hydrogel spheres aligned perpendicular to $\boldsymbol{E}_{ext}$.

Figure 4.6: Experiment results of the hydrogel dimer with three values of gap width d placed in front of a $2.45\,\mathrm{GHz}$ antenna, where $E_{ext} = 100\,\mathrm{V/cm}$ and the exposure time is $10\,\mathrm{s}$, based on Lin *et al.* [1], Fig. 7a and Fig. 7b.

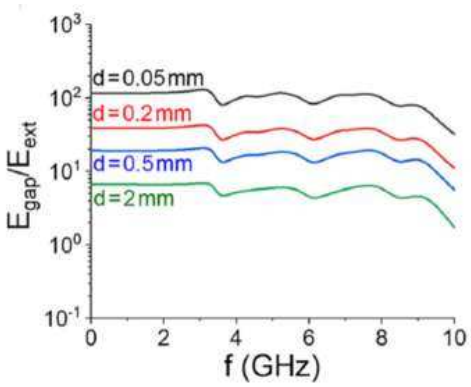

(a) Simulated gap electric field amplitude E_{gap}/E_{ext} in *log* scale.

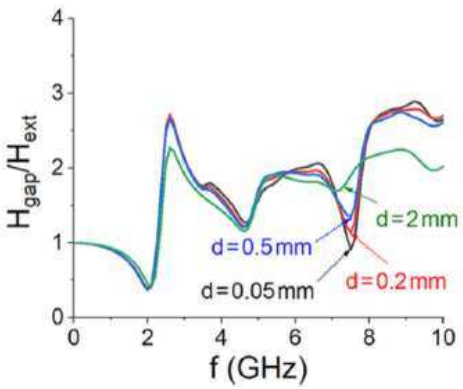

(b) Simulated gap magnetic field amplitude H_{gap}/H_{ext} in *linear* scale.

Figure 4.7: Simulated gap field amplitudes as functions of frequency for different gap widths d, based on Lin *et al.* [1], Fig. 5a and Fig. 5b.

doi:10.6342/NTU202300933

Chapter 5

Conclusion

This thesis consists of three parts. In Chapter 2, the analytic solutions for resonant modes of a dielectric spherical resonator are derived. Besides, the field patterns for first few modes are presented to visualize the field properties of different n, m, and q.

In Chapter 3, the behavior of a dielectric sphere incident by a uniform $2.45\,\mathrm{GHz}$ plane wave is studied. It is shown that there are three regimes based on the dimension of the dielectric sphere. In the first regime ($R \ll \lambda_{water}$), the interior field is weak and uniform. In the second regime ($\lambda_{water}/2 < R < \delta$), the resonant effect becomes significant. The interior field strength and distribution are thus highly dependent on the radius, while generally stronger and more uneven than those in the first regime. In the third regime ($R > \delta$), the interior field strength becomes weaker as R increases due to field attenuation. The field uniformity increases since high-order resonant modes overlap inside the sphere.

In Chapter 4, a paper about the behavior of a water dimer incident by a uniform plane wave [1] is reviewed. It is evidenced that the sparks between two closely spaced dielectric sphere are not caused by the resonance, but the polarization charge shielding effect. The fact that it is not an electromagnetic phenomenon but a electrostatic one is consistent with a further research by Liu *et al.* [10], in which the authors show that there is an attractive force between dielectric spheres. Moreover, it is mentioned in Chapter 4 that the orientation of the water dimer affects the temperature distribution in microwave heating, also due to the

doi:10.6342/NTU202300933

polarization charge shielding effect. Further researches of microwave heating for dielectric objects with asymmetric shapes show that the orientation of the samples also plays an important role in temperature distribution [29, 30].

In summary, this thesis investigates the interior and exterior field properties as dielectric sphere(s) incident by a plane wave. Hopefully it gives some basical understanding to microwave dielectric heating, and is useful for further researches.

doi:10.6342/NTU202300933

Appendix A

Helmholtz Equation and Its Solution

In this chapter, two kinds of helmholtz equation are discussed, scalar one and vector one, both of which are useful in Section 2.1.

A.1 Scalar Helmholtz Equation and Its Solution

The scalar Helmholtz equation is given by the linear partial differential equation

$$\left(\nabla^2 + k^2\right)\psi = 0 \tag{A.1}$$

where $\psi \equiv \psi(r, \theta, \phi)$ is a scalar eigenfunction. Chu [31] shows that using separation of variables, the scalar eigenfunction ψ can be expressed as $\psi = R(r)\Theta(\theta)\Phi(\phi)$, then Eq. (A.1) becomes

$$r^2 \sin^2\theta \frac{R''}{R} + 2r\sin^2\theta\frac{R'}{R} + \sin^2\theta\frac{\Theta''}{\Theta} + \sin\theta\cos\theta\frac{\Theta'}{\Theta} + \frac{\Phi''}{\Phi} + k^2 r^2 \sin^2\theta = 0\,. \tag{A.2}$$

Since ϕ only occurs in the Φ''/Φ term, it can be solved first, i.e.,

$$\frac{\Phi''}{\Phi} + m^2 = 0 \tag{A.3}$$

where m is some constant. Thus, Φ is of the form

$$\Phi \sim e^{im\phi}\,. \tag{A.4}$$

doi:10.6342/NTU202300933

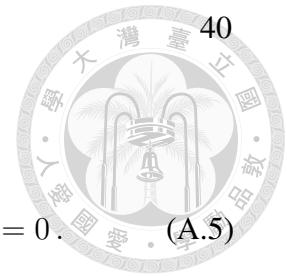

Substituting Eq. (A.4) into Eq. (A.2), it becomes

$$\frac{r^2}{R}\left(R'' + \frac{2R'}{r} + k^2 R\right) + \frac{1}{\Theta}\left(\Theta'' + \cot\theta\,\Theta' - \frac{m^2}{\sin^2\theta}\Theta\right) = 0\,. \tag{A.5}$$

Since r only occurs in the first term and θ only occurs in the second term, two terms can be treated separately. Let the first term equals some constant $n(n+1)$. Hence,

$$R'' + \frac{2R'}{r} + \left[k^2 - \frac{n(n+1)}{r^2}\right]R = 0\,; \tag{A.6}$$

$$\Theta'' + \cot\theta\,\Theta' + \left[n(n+1) - \frac{m^2}{\sin^2\theta}\right]\Theta = 0\,. \tag{A.7}$$

The solutions to Eq. (A.6) are linear combinations of spherical bessel functions $j_n(kr)$ and $y_n(kr)$, while the solutions to Eq. (A.7) are linear combinations of associated Legendre polynomials $P_n^m(\cos\theta)$ and $Q_n^m(\cos\theta)$. Thus,

$$R \sim \left\{\begin{matrix} j_n(kr) \\ y_n(kr) \end{matrix}\right\}; \tag{A.8}$$

$$\Theta \sim \left\{\begin{matrix} P_n^m(\cos\theta) \\ Q_n^m(\cos\theta) \end{matrix}\right\}. \tag{A.9}$$

The general solutions of ψ are given by Eqs. (A.4)(A.8) and (A.9), and specific ones can be obtained by applying boundary conditions.

A.2 Vector Helmholtz Equation and Its Solution

The vector Helmholtz equation is given by the linear partial differential equation

$$\left(\nabla^2 + k^2\right)\boldsymbol{\psi} = 0 \tag{A.10}$$

where $\boldsymbol{\psi}$ is a vector eigenfunction. Since the solution Chapter 2 deals with is a wave function, the vector wave equation should be also satisfied, i.e.,

$$\boldsymbol{\nabla} \times (\boldsymbol{\nabla} \times \boldsymbol{\psi}) - k^2\boldsymbol{\psi} = 0\,. \tag{A.11}$$

doi:10.6342/NTU202300933

Collin [32] shows that ψ can be separated into transverse eigenfunction $\boldsymbol{F}$ and longitudinal eigenfunction $\boldsymbol{L}$, where they satisfy

$$\boldsymbol{\nabla} \cdot \boldsymbol{F} \equiv 0, \quad \boldsymbol{\nabla} \times \boldsymbol{F} \neq 0\,; \tag{A.12a}$$

$$\boldsymbol{\nabla} \times \boldsymbol{L} \equiv 0, \quad \boldsymbol{\nabla} \cdot \boldsymbol{L} \neq 0\,. \tag{A.12b}$$

For spherical coordinate system, the solutions can be generated from the scalar function ψ of the scalar Helmholtz equation, which is given by Eqs. (A.4)(A.8) and (A.9). The longitudinal function can be obtained from the gradient of ψ, i.e.,

$$\boldsymbol{L} = \boldsymbol{\nabla}\psi\,, \tag{A.13a}$$

while the transverse function consists of two sets of solutions, $\boldsymbol{M}$ and $\boldsymbol{N}$, where

$$\boldsymbol{M} = \boldsymbol{\nabla} \times (r\psi)\hat{\boldsymbol{r}}\,; \tag{A.13b}$$

$$\boldsymbol{N} = \frac{1}{k}\boldsymbol{\nabla} \times \boldsymbol{M}\,. \tag{A.13c}$$

Similarly, boundary conditions should be applied to obtain specific solutions.

doi:10.6342/NTU202300933

Reference

[1] M. S. Lin, L. C. Liu, L. R. Barnett, Y. F. Tsai, and K. R. Chu, "On electromagnetic wave ignited sparks in aqueous dimers," *Physics of Plasmas*, vol. 28, no. 10, 2021. v, 2, 3, 30, 31, 32, 33, 34, 35, 36, 37

[2] U. Kaatze, "Complex permittivity of water as a function of frequency and temperature," *Journal of Chemical and Engineering Data*, vol. 34, no. 4, pp. 371–374, 1989. vi, 9, 10

[3] D. W. Hall, "Microwave - a method to control herbarium insects," *Taxon*, vol. 30, no. 4, pp. 818–819, 1981. 1

[4] S. O. Nelson, P. G. Bartley, and K. C. Lawrence, "RF and microwave dielectric properties of stored-grain insects and their implications for potential insect control," *Transactions of the Asae*, vol. 41, no. 3, pp. 685–692, 1998. 1

[5] N. E. Bengtsson and T. Ohlsson, "Microwave-heating in food-industry," *Proceedings of the Ieee*, vol. 62, no. 1, pp. 44–55, 1974. 1

[6] Q. S. Guo, D. W. Sun, J. H. Cheng, and Z. Han, "Microwave processing techniques and their recent applications in the food industry," *Trends in Food Science & Technology*, vol. 67, pp. 236–247, 2017. 1

doi:10.6342/NTU202300933

[7] P. Guzik, P. Kulawik, M. Zajac, and W. Migdal, "Microwave applications in the food industry: an overview of recent developments," *Critical Reviews in Food Science and Nutrition*, vol. 62, no. 29, pp. 7989–8008, 2022. 1

[8] K. H. Brosnan, G. L. Messing, and D. K. Agrawal, "Microwave sintering of alumina at 2.45 GHz," *Journal of the American Ceramic Society*, vol. 86, no. 8, pp. 1307–1312, 2003. 1

[9] M. Oghbaei and O. Mirzaee, "Microwave versus conventional sintering: A review of fundamentals, advantages and applications," *Journal of Alloys and Compounds*, vol. 494, no. 1-2, pp. 175–189, 2010. 1

[10] L. C. Liu, M. S. Lin, and K. R. Chu, "Microwave-induced attractive force between dielectric spheres - a potential non-thermal effect in microwave sintering," *Modern Concepts in Material Science*, vol. 4, 2022. 1, 37

[11] J. M. Osepchuk, "A history of microwave-heating applications," *Ieee Transactions on Microwave Theory and Techniques*, vol. 32, no. 9, pp. 1200–1224, 1984. 1

[12] J. D. Jackson, *Classical electrodynamics*, 3rd ed. New York: Wiley, 1999, ch. 7. 1, 25, 27

[13] D. J. Griffiths, *Introduction to electrodynamics*, 4th ed. Boston: Pearson, 2013. 2

[14] J. D. Jackson, *Classical electrodynamics*, 3rd ed. New York: Wiley, 1999. 2

[15] R. A. Yadav and I. D. Singh, "Normal modes and quality factors of spherical dielectric resonators: I - shielded dielectric sphere," *Pramana-Journal of Physics*, vol. 62, no. 6, pp. 1255–1271, 2004. 2

[16] M. Pascale, G. Miano, R. Tricarico, and C. Forestiere, "Full-wave electromagnetic modes and hybridization in nanoparticle dimers," *Scientific Reports*, vol. 9, 2019. 2

doi:10.6342/NTU202300933

[17] T. Yousefi, S. A. Mousavi, M. Z. Saghir, and B. Farahbakhsh, "An investigation on the microwave heating of flowing water: A numerical study," *International Journal of Thermal Sciences*, vol. 71, pp. 118–127, 2013. 2

[18] M. Tanaka and M. Sato, "Microwave heating of water, ice, and saline solution: Molecular dynamics study," *Journal of Chemical Physics*, vol. 126, no. 3, 2007. 2

[19] D. Dallinger and C. O. Kappe, "Microwave-assisted synthesis in water as solvent," *Chemical Reviews*, vol. 107, no. 6, pp. 2563–2591, 2007. 2

[20] J. D. Jackson, *Classical electrodynamics*, 3rd ed. New York: Wiley, 1999, ch. 9. 4

[21] ——, *Classical electrodynamics*, 3rd ed. New York: Wiley, 1999, ch. 8. 5

[22] M. Abramowitz and I. A. Stegun, *Handbook of mathematical functions, with formulas, graphs, and mathematical tables*. New York: Dover Publications, 1965, ch. 10. 20

[23] R. F. Harrington, *Time-harmonic electromagnetic fields*. New York: IEEE Press: Wiley-Interscience, 2001, ch. 6. 20, 22

[24] K. R. Chu, *Classical Electrodynamics II Lecture Notes*. Taipei: Department of Physics, National Taiwan University, 2021, ch. 7. 23

[25] T. A. Beu, *Introduction to numerical programming: a practical guide for scientists and engineers using Python and C/C++*. Boca Raton: CRC Press, Taylor & Francis Group, 2015, ch. 10. 23

[26] J. D. Jackson, *Classical electrodynamics*, 3rd ed. New York: Wiley, 1999, ch. 4. 24

[27] K. R. Chu, *Classical Electrodynamics I Lecture Notes*. Taipei: Department of Physics, National Taiwan University, 2019, ch. 4. 24

[28] H. K. Khattak, P. Bianucci, and A. D. Slepkov, "Linking plasma formation in grapes to microwave resonances of aqueous dimers," *Proceedings of the National Academy*

doi:10.6342/NTU202300933

of Sciences of the United States of America, vol. 116, no. 10, pp. 4000–4005, 2019. 30

[29] M. S. Lin, S. M. Lin, W. Y. Chiang, L. R. Barnett, and K. R. Chu, "Effects of polarization-charge shielding in microwave heating," *Physics of Plasmas*, vol. 22, no. 8, 2015. 38

[30] Y. F. Tsai, L. R. Barnett, H. H. Teng, C. C. Ko, and K. R. Chu, "A study of some inherent causes for non-uniform microwave heating," *Physics of Plasmas*, vol. 24, no. 10, 2017. 38

[31] K. R. Chu, *Classical Electrodynamics I Lecture Notes*. Taipei: Department of Physics, National Taiwan University, 2019, ch. 3. 39

[32] R. E. Collin, I. Antennas, and P. Society., *Field theory of guided waves*, 2nd ed. New York: IEEE Press, 1991, ch. 2. 41

doi:10.6342/NTU202300933